Development in Utilizing Singlet Fission and Triplet-Triplet Annihilation to Improve Solar Cell Efficiency

by

Tony Chang-Chi Wu

Submitted to the Department of Electrical Engineering and Computer Science
in partial fulfillment of the requirements for the degree of

Doctor of Philosophy in Electrical Engineering and Computer Science

at the

MASSACHUSETTS INSTITUTE OF TECHNOLOGY

February 2018

Signature redacted

Author .....
Department of Electrical Engineering and Computer Science
October 17, 2017

Signature redacted

Certified by.....
Marc A Baldo
Professor of Electrical Engineering and Computer Science
Thesis Supervisor

Signature redacted

Accepted by .....
Leslie A. Kolodziejski
Professor of Electrical Engineering and Computer Science
Chair, Department Committee on Graduate Students

Development in Utilizing Singlet Fission and Triplet-Triplet Annihilation to Improve Solar Cell Efficiency

by

Tony Chang-Chi Wu

Submitted to the Department of Electrical Engineering and Computer Science
on October 17, 2017, in partial fulfillment of the
requirements for the degree of
Doctor of Philosophy in Electrical Engineering and Computer Science

Abstract

Our main energy source are burning fossil fuels. Solar energy is a clean, sustainable energy source that does not emit greenhouse gas that causes global warming. In this thesis, singlet fission and triplet-triplet annihilation would be discussed and studied to increase solar cell power conversion efficiency.

Singlet fission splits a singlet exciton into two lower energy triplet excitons. This energy down conversion is efficient and have shown near 200% triplet exciton yield. With energy down conversion, thermalization loss in solar cell could be reduced. We have shown singlet fission in tetracene, a suitable down conversion fission material to pair with silicon solar cell, up to 127% of internal quantum yield. To integrate tetracene as the energy down converter for silicon, we have demonstrated triplet exciton transfer from tetracene to silicon with WN_x passivation. To show triplet exciton transfer, a spectrally resolved magnetic field effect measurement setup was designed and built.

We have also demonstrated a metal-free, solid state optical up conversion system. This is in contrast with most optical up conversion system that uses heavy metal for triplet generation and are limited to solution fabrication based on material restrictions. The novel optical up conversion system provided cheaper material choices as well as better fabrication freedom and potentially longer device operation lifetime.

Thesis Supervisor: Marc A Baldo
Title: Professor of Electrical Engineering and Computer Science

Acknowledgments

This thesis is done with support from many people in both academic colleagues and outside of research. The most important people to appreciate is my PhD advisor, professor Marc Baldo. He has guided me during my ups and downs, excitements and frustrations in research. He is also patient on my wild ideas and wisely point me to the right directions when I was lost in research. Thank you very much for all the enlightenment, Marc.

Many labmates in the SEE group have taught me and provided me great suggestions on research over the years. Thank you Carlijn, Jiye, Priya for teaching me on crystal growth and device fabrications. I also appreciate Nick, Shane, Phil, Matthias, Dan, Brian, Dong-Gwang, Jean Anne for discussing about research, science and occasionally sports. I would also like to specially thank Markus and Kurt for all the help on the difficult triplet transfer project. The project would not be possible with your help.

During my time at MIT, there has been ups and downs. I would like to thank my families and friends in both Taiwan and Boston. Thank you for the support all the years that push me through my PhD.

Contents

List of Figures

Chapter 1

Introduction

The first two chapters will provide introduction and the background for the results in this thesis. Chapter 2 will briefly introduce the physics organic semiconductors and its usage in organic photovoltaics (OPV). In chapter 3, I will discuss the background on singlet fission and triplet-triplet annihilation [12, 13, 14], which is an essential part of this thesis.

From chapters 4 to 6, I will be showing my results in singlet fission and triplet-triplet annihilation. In chapter 4, I will characterize the efficiencies of singlet fission in tetracene. The realization of efficient fission in tetracene extended to the project on demonstrating triplet exciton transfer from tetracene to silicon in chapter 6. These results are the first steps for creating a down converter for silicon solar cells. In chapter 5, I will show a novel optical up conversion device structure that does not require solution processing and heavy metals.

Chapter 2

Organic Semiconductors

2.1 Semiconductors

Semiconductor materials have conductivities in between a conductor and an insulator. The conducting property is due to the reason that semiconductor material has smaller energy bandgap compared to insulators, which is the gap between conduction band (mobile electrons) and valence band (mobile holes, vacant electrons). Conductivity in a semiconductor can be altered by introducing impurities (doping) or gating with applied electric field. Doping and gating can change the conductivity and majority carrier type in the material, where n-type indicates the material containing mostly free electrons and p-types containing mostly free holes. By placing p-type and n-type materials together, a p-n junction is created. p-n junctions are the fundamental elements for semiconductor devices, which includes integrated circuits (in CPU), photovoltaics and light-emitting diodes (LEDs).

In figure 2-1, the energy levels and band structures of a p-n junction is plotted. The Fermi level is the energy level where the electrons in the material are filled up to, or more precisely, there will be 50% chance of electrons occupying the level at thermodynamic equilibrium. In a system where charges are free to move, the energy bands will bend until Fermi levels are in equilibrium. The n-type material has a higher Fermi level (closer to the conduction band, more free electrons) compared to p-type (closer to the valence band, more free holes). In a p-n junction, this creates

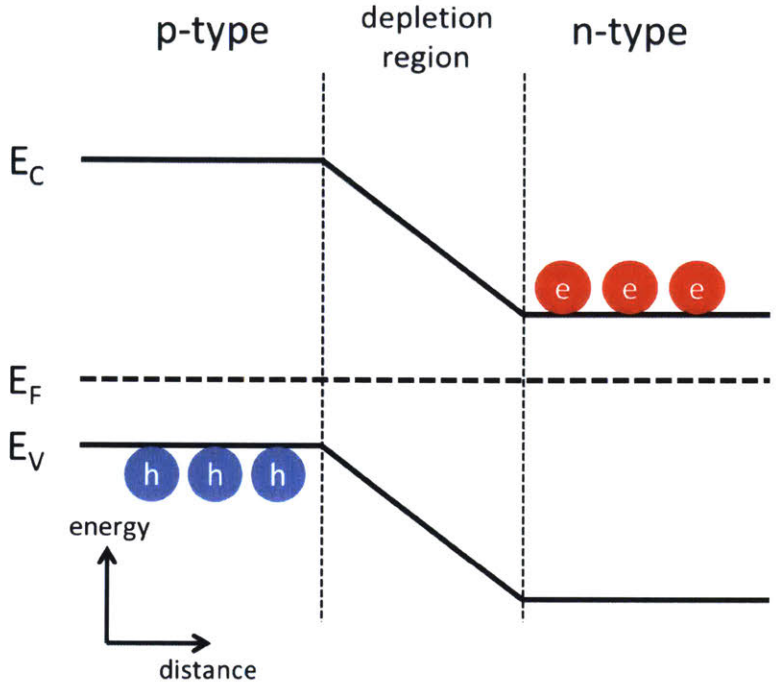

Figure 2-1: Conduction Band, Valence Band and p-n Junction. E_C is the conduction band energy; E_V is the valence band energy; E_F is the Fermi level. The Fermi level differences in p-type and n-type semiconductors causes the electrons to diffuse from n-type to p-type and holes to diffuse vice versa. After the Fermi levels balance, there will be a depletion region with built in potential between n-type and p-type materials.

a Fermi level difference, causing the electrons to diffuse from n-type to p-type and holes to diffuse vice versa. After the Fermi levels balance, there will be a depletion region with a built-in potential between n-type and p-type materials. This creates interesting properties for electrical devices. For example, under forward bias (using the figure as an example, the left side is connected to a higher voltage than the right), the depletion region will decrease and eventually thin enough for the electrons and holes to tunnel across the junction and recombine. There is a rapid current increase when the forward bias is larger than a threshold voltage. However, if the p-n junction is reversed biased, the depletion region will increase and minimal current will flow through.

Photovoltaics utilize the depletion region to collect photocurrent. In figure 2-2, the photon absorbed may excite an electron from the valence band. The carriers

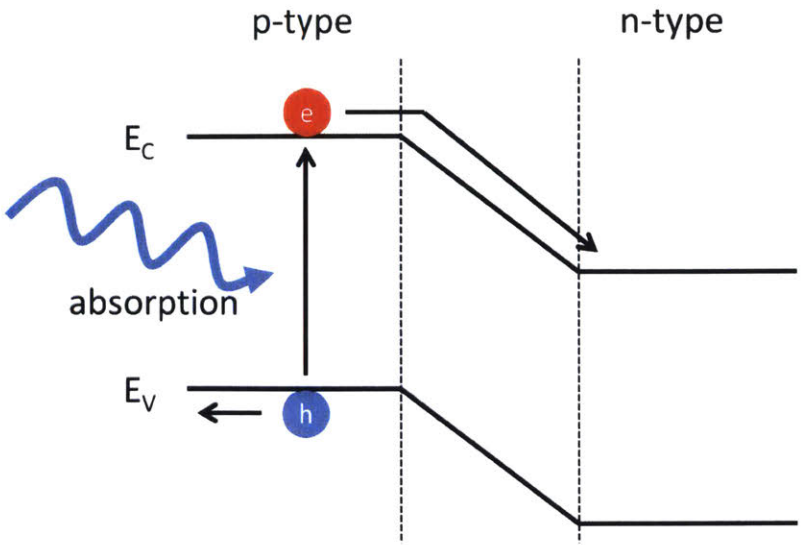

Figure 2-2: Simple Photovoltaic Diagram. Photovoltaics utilize the depletion region to collect photocurrent. The semiconductor absorbs and an electron are excited from the valence band. The carriers then diffuse to the junction and swept to the sides by the built-in potential.

can then diffuse to the junction and split by the built-in potential at the depletion region. The carriers diffusion lengths in the material are important parameters in the determination of the overall solar cell power conversion efficiency.

2.2 Semiconductors with Organic Molecules

Organic semiconductors are based on organic molecules or polymers which mainly consist of carbon, hydrogen and occasionally oxygen, nitrogen, sulfur, etc. This is in contrast to semiconductors where the crystals are based on atoms. In the crystals, the orbitals of the valence electrons of the atoms overlap. For a two atoms system, the overlapped orbitals splits into a higher and lower energy molecular orbitals. With N multiple atoms, the molecular orbitals splits into N higher energy levels and N lower energy levels. Due to many atoms in a semiconductor material, the high and low energy levels could be viewed as conduction bands and valence bands. Organic molecule's valence orbitals are typically more localized because molecules are bound together in a solid by Van der Waals force. Hence, some properties in organic semi-

conductors should be treated differently.

2.2.1 Molecular Orbitals

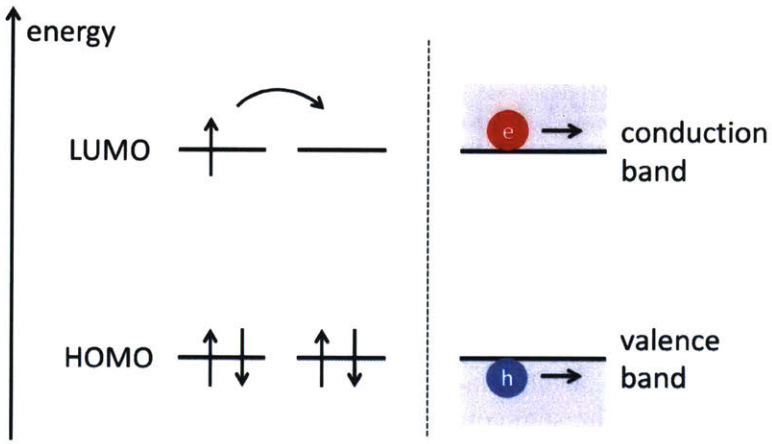

Figure 2-3: Organic semiconductor and semiconductor comparisons. On the left are the energy levels for organic molecules; Highest Occupied Molecular Orbitals (HOMO) and Lowest Unoccupied Molecular Orbitals (LUMO). The electrons or holes in organic molecules are usually localized and transport through hopping. In comparison, the right are the semiconductor conduction bands and valence bands, where electrons and holes move freely.

In an organic molecule, the energy levels of interest are the Highest Occupied Molecular Orbitals (HOMO) and the Lowest Unoccupied Molecular Orbitals (LUMO). HOMO levels are the highest electron energies for molecules in ground states, and the LUMO levels are for additional electrons to occupy. These energy levels are similar to the valence bands and conduction bands. However, organic molecular crystals are formed from the weak interaction of Van der Waals bonds. Thus, the HOMO and LUMO energy levels are treated as localized in the molecules instead of viewing them as delocalized conduction and valence bands. Therefore, the electrons or holes in organic molecules move in the material through hopping instead of conduction.

To understand how the electrons occupy energy levels, we would need to understand the states of identical particles. In quantum mechanics, a particle state could be represented as $|n\rangle$ that includes spacial, angular momentum, spins, etc. We first start from understanding a simple two particle system, which can then be extended

to multiple particles system. The state of two particle system can be expressed as $|\psi(n_1, n_2)\rangle$ where the n_1 represent the states for particle 1 and n_2 for particle 2. Assuming a swapping operator P that switches the states of particle 1 and 2, then $P|\psi(n_1, n_2)\rangle = |\psi(n_2, n_1)\rangle$. For two states to be physically equivalent under measurements, the wavefunctions should only be different by a factor of complex number $|\psi\rangle = \alpha|\psi\rangle$. Therefore, the states of identical two particle system should satisfy,

$$P|\psi(n_1, n_2)\rangle = \alpha|\psi(n_1, n_2)\rangle. \tag{2.1}$$

From equation 2.1, the simple expression of two particle system $|\psi(n_1, n_2)\rangle = |n_1\rangle|n_2\rangle$ cannot describe an identical two particle system because $|n_2\rangle|n_1\rangle \neq \alpha|n_1\rangle|n_2\rangle$ for any states n. To express an identical two particle system with n_1 and n_2, we assume the state $|\psi\rangle$ is the linear combination of the possible joint states, then it can be expressed as,

$$|\psi(n_1, n_2)\rangle = a|n_1\rangle|n_2\rangle + b|n_2\rangle|n_1\rangle. \tag{2.2}$$

From equations 2.1 and 2.2,

$$a|n_2\rangle|n_1\rangle + b|n_1\rangle|n_2\rangle = \alpha(a|n_1\rangle|n_2\rangle + b|n_2\rangle|n_1\rangle) \tag{2.3}$$

$$\Rightarrow \alpha a = b, \alpha b = a. \tag{2.4}$$

From solving the simple relations, $\alpha = \pm 1$. a and b can then be solved for respective α with normalization constraints. With the constants, the states to describe identical two particle systems is expressed as,

$$|\psi(n_1, n_2)_+\rangle = \frac{1}{\sqrt{2}}\left(|n_1\rangle|n_2\rangle + |n_2\rangle|n_1\rangle\right), \tag{2.5}$$

$$|\psi(n_1, n_2)_-\rangle = \frac{1}{\sqrt{2}}\left(|n_1\rangle|n_2\rangle - |n_2\rangle|n_1\rangle\right). \tag{2.6}$$

Particles in identical particles systems that are symmetric, described by 2.5, are called Bosons, where as the particles that are anti-symmetrical, described by 2.6, are Fermions. One big difference between Bosons and Fermions is the symmetry.

In equation 2.6, n_1 cannot equal n_2 for the Fermions or else $\langle k_-|k_-\rangle = 0$. Hence, the Pauli exclusion principle indicates that no two Fermions may occupy the same state. However, Bosons are not constrained by the Pauli exclusion principle. Common Fermions include electrons or protons, where photons are Bosons.

The state of an electron can be represented as

$$|n\rangle = |\psi(x)\chi\rangle, \tag{2.7}$$

where $\psi(x)$ is the spacial wave function and χ is the spin function. Thus, for electrons to occupy the same energy level $\psi_1 = \psi_2$, the spin function of the electrons must be different due to the Pauli exclusion principle. Because the electrons only have spins $\pm\frac{1}{2}$, only two electrons may occupy the same energy level and the spins of those electrons must be $\frac{1}{2}$ and $-\frac{1}{2}$. Therefore in the ground state of an organic molecule, the HOMO energy level has two electrons with spins $\frac{1}{2}$ and $-\frac{1}{2}$. The spin eigenstates calculations are based on Quantum Mechanics Books written by Shankar [15] and Sakurai [16].

2.3 Excited States in Organic Molecules

Excitons are electron hole pairs in semiconductors. Organic materials have low dielectric constants in organic materials. Thus, the excitons usually have large binding energy, typically on the order of 0.5eV [17] compared to excitons in semiconductors. Also, due to weak interactions between the molecules, the excitons are localized to one or few molecules. Based on the reasons, the excitons in organic semiconductors are best treated as localized excited states.

2.3.1 Spins in Excited states

The organic molecule may absorb a photon and promote an electron from HOMO energy level to LUMO energy level. Based on the equation 2.7 in section 2.2.1, since the two electrons does not have the same spatial wave functions, the excited states

can have 4 possible spin combinations:

$$|\uparrow\uparrow\rangle = |m_{s1} = \frac{1}{2}, m_{s2} = \frac{1}{2}\rangle \tag{2.8}$$

$$|\uparrow\downarrow\rangle = |m_{s1} = \frac{1}{2}, m_{s2} = -\frac{1}{2}\rangle \tag{2.9}$$

$$|\downarrow\uparrow\rangle = |m_{s1} = -\frac{1}{2}, m_{s2} = \frac{1}{2}\rangle \tag{2.10}$$

$$|\downarrow\downarrow\rangle = |m_{s1} = -\frac{1}{2}, m_{s2} = -\frac{1}{2}\rangle \tag{2.11}$$

In the equations above, m_s is the secondary spin quantum number of an electron that describes the spin projected in the z direction. It could be $\pm\frac{1}{2}$ for electrons. The total spin of the electron is $s = \frac{1}{2}$. However, the states in the above equations are not eigenvectors for S^2 (operator that measures total spin). The eigenvectors of the excited states that satisfies both S^2 and S_z are then calculated and expressed as,

$$|s = 0, m_s = 0\rangle = \frac{1}{\sqrt{2}}(|\uparrow\downarrow\rangle - |\downarrow\uparrow\rangle) \tag{2.12}$$

$$|s = 1, m_s = 1\rangle = |\uparrow\uparrow\rangle \tag{2.13}$$

$$|s = 1, m_s = 0\rangle = \frac{1}{\sqrt{2}}(|\uparrow\downarrow\rangle + |\downarrow\uparrow\rangle) \tag{2.14}$$

$$|s = 1, m_s = -1\rangle = |\downarrow\downarrow\rangle. \tag{2.15}$$

The eigenstates are categorized into two spin states, one singlet states with total spin $s = 0$ and three triplet states with spin $s = 1$. These are the eigenstates for the excited states. The ground state can only be a singlet state due to the Pauli exclusion principle. Singlet and triplet configuration of the excited state are plotted in figure 2-4.

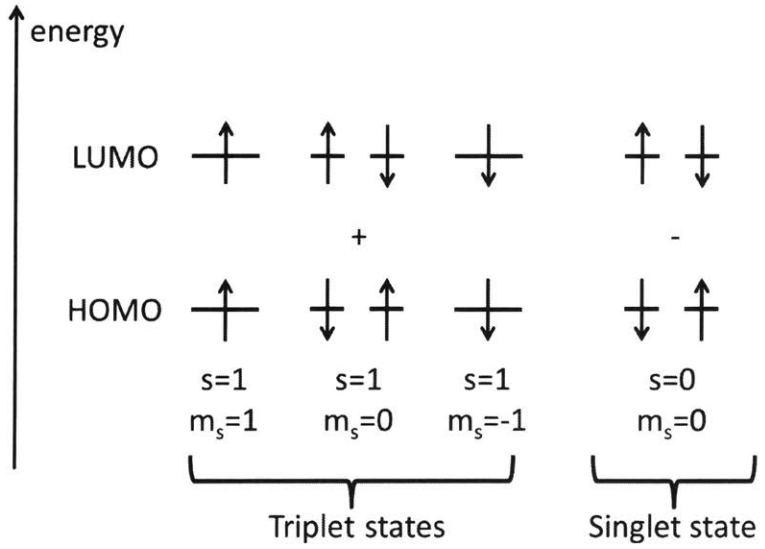

Figure 2-4: Spin of the Excited States. In a system of two identical particles, the energy states can be represented as one singlet state and three triplet states.

2.3.2 Selection Rule

From the equations 2.12 - 2.15, the singlet states are anti-symmetric under particle exchange while the triplet excitons are symmetric. This is important to determine whether if a electric dipole transition is allowed. Under Fermi golden rule, the transition between an excited state and the singlet ground state can be written as,

$$\langle k_{excited}|\hat{d}|k_{ground}\rangle = \langle \chi_{excited}|\chi_{ground}\rangle\langle \psi_{excited}|\hat{d}|\psi_{ground}\rangle \tag{2.16}$$

where $\hat{d}$ is the dipole transition moment. From the first term of the right hand side, the spin transitions can only be non-zero if the spin wave functions are the same. If one is a triplet state and the other is singlet state, the integral would be zero due to anti-symmetry of the product. Since the ground state of a molecule is typically a singlet, only singlet excited states can emit photons or be created from ground states through absorbing photons. The triplet states are usually inaccessible and called dark state due to their forbidden transitions.

From equation 2.6, we know that the two Fermions are anti-symmetric, thus the spatial wave function of a singlet state is symmetric while the triplet state's spatial

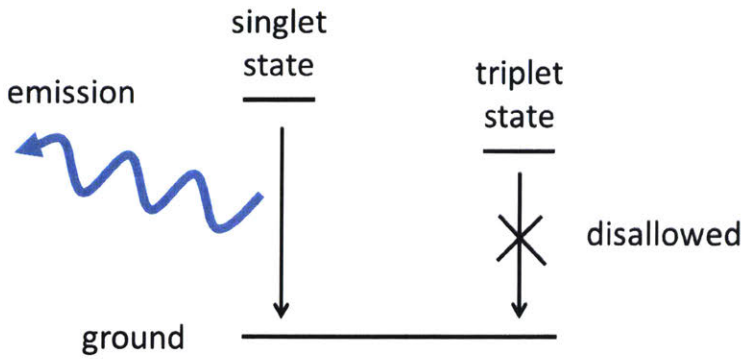

Figure 2-5: Singlet and Triplet Excitons in Organic Molecules. Due to selection rules, singlet excitons are emissive while the triplet excitons are not emissive nor absorptive. The triplet excited state also has lower energy compared to singlet state due to anti-symmetric wave functions. The anti-symmetric spatial wave function reduces the electron-electron repulsion energy in a molecules.

wave function is anti-symmetric. The anti-symmetry of the triplet state spatial wave function reduces the electron-electron repulsion energy in a molecules, reducing its energy compared to the singlet excited states.

2.3.3 Exciton Transport

Excitons are strongly localized within the organic semiconductor materials. In figure 2-6, we show two possible ways for an exciton to transport in a material. The first is Förster resonance energy transfer (FRET) [2]. Förster transfer is an energy transfer through a non-radiative dipole-dipole coupling. This transfer requires the molecule states to be emissive and absorptive. Thus, the singlet excitons may transport through Förster transfers while triplets generally do not. Another transport mechanism is Dexter transfer [1], where an electron on the donor LUMO jumps to the acceptor LUMO and the electron from the acceptor HOMO simultaneously jumps to the donor, effectively moving the exciton. This does not require the molecular states to be radiative. The mechanism, however, requires the wave functions between the organic molecules to overlap for efficient transfer.

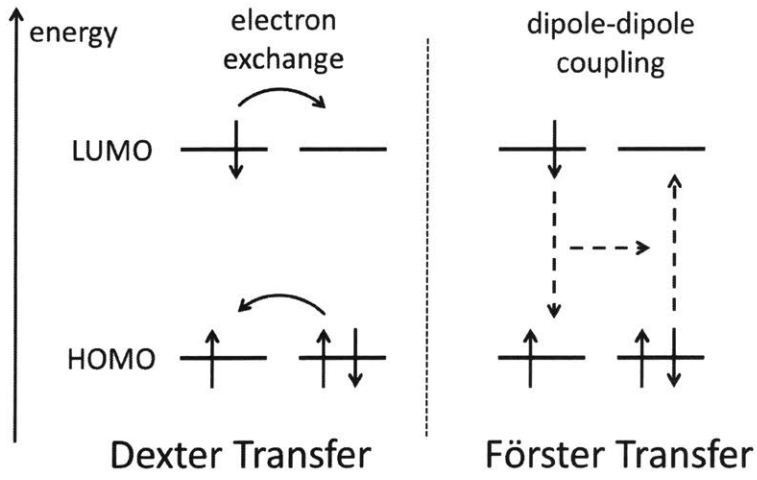

Figure 2-6: Exciton Transport. On the left is Dexter transfer [1], where the electrons in donor LUMO jumps to the acceptor LUMO and the electrons from the accepter HOMO jumps to the donor, effectively moving the exciton. On the right is the Förster resonance energy transfer (FRET) [2]. Förster transfer is an energy transfer through a non-radiative dipole-dipole coupling, requiring the molecule states to be emissive and absorptive.

2.4 Organic Photovoltaics (OPV)

Organic photovoltaics are solar cells where the materials are organic molecules instead of semiconductors. The basic device structure of an organic photovoltaic consists of a donor and acceptor material where the energies levels $E_{D,HOMO} > E_{A,HOMO}$ and $E_{D,LUMO} > E_{A,LUMO}$ (D = donor energies, A = acceptor energies). Charge transfer states, where the electrons and holes are on different molecules, are formed at the donor-acceptor interface. The energy of the charge transfer state $E_{CT} = E_{A,LUMO} - E_{D,HOMO}$.

Photons absorbed in the organic material can create excitons. The excitons then propagate to donor-acceptor interface and form the charge-transfer state. Once the charge-transfer state is formed, the excitons may then dissociate into electrons on the acceptor material and holes on the donor. The carriers can then diffuse to the electrodes and get collected as photocurrent. Figure 2-7 is a simple OPV schematic.

The operation of an OPV is similar to a semiconductor solar cell. The organic donor materials are similar to p-type materials whereas the acceptors are n-type

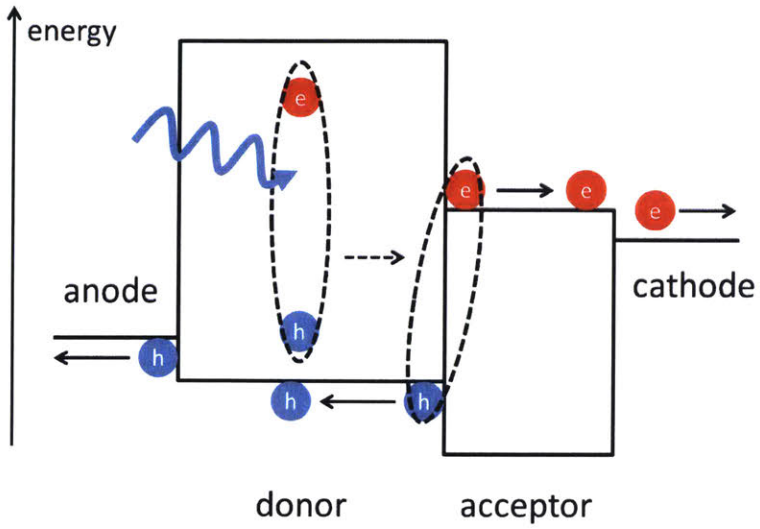

Figure 2-7: Schematics for Organic Photovoltaic. The HOMO LUMO energy levels of donor and acceptor in an organic photovoltaic are plotted. The excitons created in the material can diffuse to the donor-acceptor interface and transfer to the charge-transfer state. Once the charge-transfer state are formed, the excitons then dissociate into electrons on acceptor material and holes on donor. The carriers transport to the electrodes and get collected as photocurrent.

materials. Recently, the power conversion efficiency in a OPV have reached 11.5% [18]. In comparison, silicon solar cell have reached 26% power conversion efficiency [19]. OPV usually suffers from low fill factors (below 70%) and short device lifetime.

In chapter 3, I will discuss more about energy down conversion and up conversion mechanisms called singlet fission and triplet-triplet annihilation that occur in organic semiconductors. The chapter will show the possibility of utilizing these mechanisms to increase solar cell efficiencies.

Chapter 3

Singlet Fission and Triplet-Triplet Annihilation

As mentioned in chapter 2, the current silicon solar cell power conversion efficiency record is 26.0% [19] and the record for organic photovoltaics is 11.5% [18]. The fundamental limits for solar cell power conversion efficiency (PCE) will be discussed in this section. In this section, I will show some of the mechanisms that could overcome these limits.

3.1 Down Conversion and Up Conversion

Down converison and up conversion are some mechansims that may overcome the PCE limit that will be studied in this thesis. To understand the limits, in this section I will show the theoretical limits of a single junction solar cells imposed by the Shockley-Queisser limit [3].

3.1.1 Shockley-Queisser Limit

Energy losses in a single-junction solar cell are shown in figure 3-1 based on the Shockley-Queisser limit [3]. The first main loss is from non-absorption. For incident photon energies E_{hv} that are lower than the band gap energy E_g, the photons are not

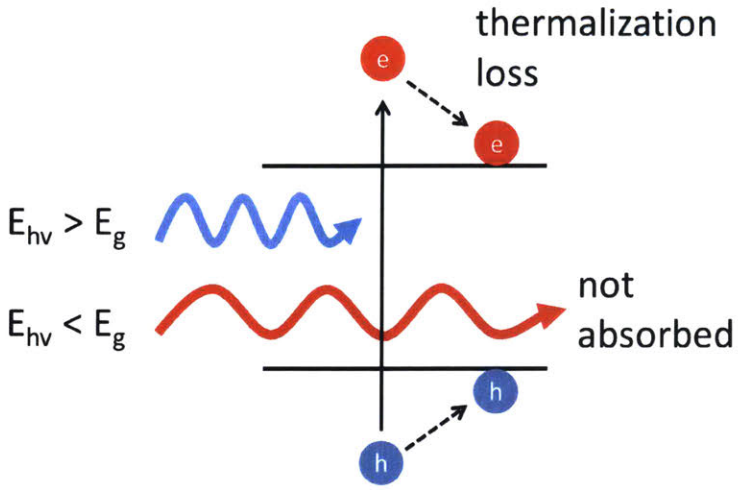

Figure 3-1: Main Energy Losses in the Shockley-Queisser Limit. The first main loss is from non-absorption. For incident photon energies E_{hv} that are lower than the band gap energy E_g, the photons are not absorbed. The second loss is from thermalization. For photons with energy E_{hv} higher than E_g, the photons can be absorbed, creating electrons and holes. However, the carriers will relax to the band gap energy, losing excess energy. An additional loss comes from carrier extraction. Practically, it is impossible to extract the carriers with the potential difference of the band gap. The solar cell will operate at a voltage lower than the $\frac{E_g}{e}$. This depends on multiple factors such as temperature and material radiative efficiency.

absorbed. The second loss is from thermalization. For photons of energy E_{hv} higher than E_g, the photons can be absorbed, creating electrons and holes. However, the carriers will relax to the band gap energy, losing their excess energy. An additional loss comes from carrier extraction. Practically, it is impossible to extract the carriers with the potential difference of the band gap. The solar cell will operate at a voltage lower than the $\frac{E_g}{e}$, where e is the charge of an electron. This depends on multiple factors such as temperature and material radiative efficiency. Decreasing band gap energy E_g increases photon absorption but also increases thermalization losses. The trade off between thermalization and absorption decides the optimized efficiency band gap.

In figure 3-2a, the PCE limit for each band gap energy E_g is calculated. Based on the losses shown in figure 3-1, there will be an optimal band gap energy E_g that has a maximum PCE. The maximum PCE for a single junction solar cell is 33.7%

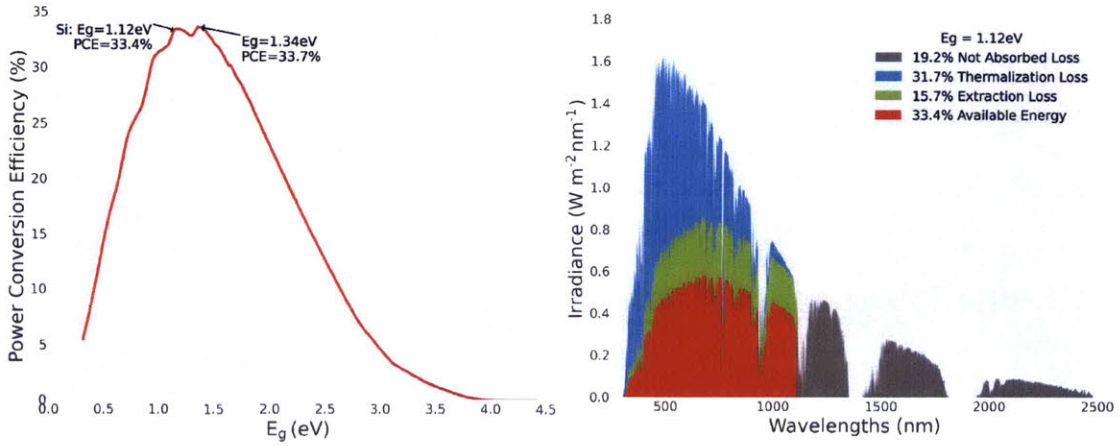

(a) Efficiency Losses for Maximum PCE in Singlet Junction Solar Cell.

(b) Maximum PCE for Single Junction Solar Cells.

Figure 3-2: Shockley-Queisser Limit. (a) Detailed balance limit for single junction solar cells. Due to the trade off, a single junction solar cell has an optimum band gap energy E_g that has maximum power conversion efficiency (PCE). The maximum PCE is 33.7% for $E_g = 1.34$ eV. As a comparison, silicon solar cell has a maximum PCE of 33.4% $E_g = 1.12$eV. [3] (b) Efficiency losses for a single junction solar cell with $E_g = 1.34$eV. From the solar spectrum and its contribution to PCE, there is 29.7% loss due to photons that are not absorbed, 23.3% loss from thermalization and 13.3% from extraction loss. This leaves 33.7% of available energy [3]. The solar energy spectrum is from NREL [4].

with a 1.34 eV band gap energy. As a comparison, silicon, the second most abundant element on earth, has a band gap energy of 1.12 eV and a maximum PCE of 33.4%. The current silicon solar cell PCE record is 26% [3] [19]. In figure 3-2b, the energy losses for a solar cell with $E_g = 1.34$eV are shown relative to the solar energy spectrum. About 29.7% energy is loss due photons that are to not absorbed, 23.3% loss from thermalization and 13.3% from extraction loss.

3.1.2 Overcoming the Limit

Since the Shockley-Queisser limit is calculated for a single junction solar cell under normal operation conditions, there are multiple methods to overcome the limit. For example, concentrating the incident sun light could decrease the extraction loss due to the higher fill factor and larger open circuit voltage. Lowering the operation temperature could also decrease the extraction loss. Another way is using multiple band gap material to build a tandem solar cell. This could decrease thermalization loss and non-absorption loss. In this thesis, we focus on alternative methods used for creating a pseudo tandem solar cell, which uses energy down conversion [20, 21] and up conversion [22, 23].

Down Conversion

Photons with energy higher than the material band gap energy will have thermalization loss. Instead of relaxation, if the energy could be split and be collected separately, some of the thermalization loss could be reduced. To understand the gain with an energy down converter, this mechanism splits energy above $2E_g$ into two energies with E_g. For photon energies larger than $2E_g$, a solar cell with a down converter could collect additional E_g for the absorbed high energy photons, compared to a normal single junction solar cell. In figure 3-3a, the collected energy of the optimum down conversion solar cell is plotted. The blue area in the solar spectrum represents the additional gain if a down converter is added to the solar cell. Additionally, the higher photocurrent from down conversion also decreases the extraction loss slightly.

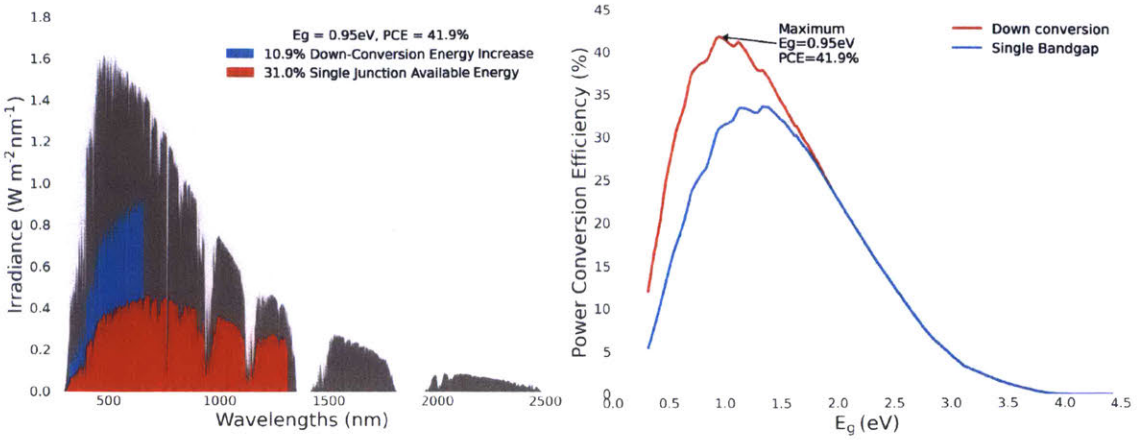

(a) Down Conversion Efficiency Increase

(b) PCE Limit with Down Conversion

Figure 3-3: Down Conversion Efficiency Spectrum and Maximum PCE Curve. (a) With down conversion, the solar cell could utilize about twice more photocurrent where the spectrum $E_{hv} > 2E_g$. Due to higher photocurrent in the device, the extraction efficiency is also slightly higher, as the blue area is marginally larger in range, which can be seen in $2E_g > E_{hv} > E_g$. (b) The improved PCE for different band gap energy. As expected, the maximum PCE 41.9% is higher than single junction solar cell maximum PCE 33.7%. Also, optimum band gap E_g = 0.95eV is lower than E_g = 1.34eV to recycle more energy in the blue region.

In figure 3-3b, PCE limits for different band gap energy are plotted. The maximum PCE for a down conversion solar cell is 41.9%, which as expected is larger then the maximum PCE of a single junction solar cell. Note that the optimum band gap for a down conversion solar cell is shifted lower to capitalize more in the high energy part of the solar spectrum with the down converter. In recent years, over 100% energy down conversion yield has been shown [24, 6, 25], making the mechanism a candidate for improving solar cell PCE.

Up Conversion

Energy up conversion is the opposite of down conversion. The up converter could merge two low energy excitation into a high energy $\frac{1}{2}E_g + \frac{1}{2}E_g \rightarrow E_g$. With an energy up converter, the solar cell could use the non-absorption part of the solar energy spectrum. In figure 3-4a, the collected energy of the optimum up conversion solar cell is plotted. The blue area in the solar spectrum represents the additional gain if

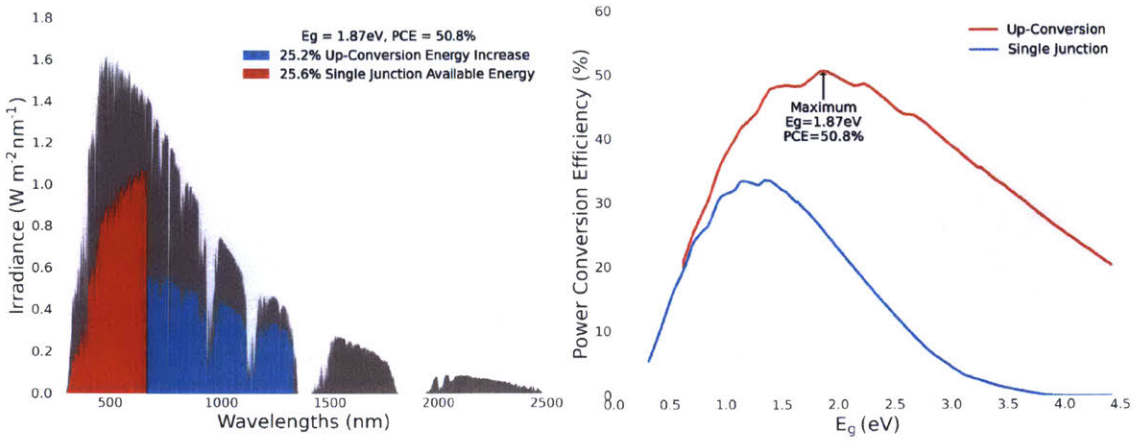

(a) Up Conversion Efficiency Increase

(b) PCE Limit with Up Conversion

Figure 3-4: Up Conversion Efficiency Spectrum and Maximum PCE Curve. (a) With up conversion, the solar cell could utilize the spectrum in $E_g > E_{hv} > \frac{E_g}{2}$. Due to higher photocurrent in the device, the extraction efficiency is also slightly higher. (b) The improved PCE for different band gap energies with up conversion. As expected, the maximum PCE 50.8% is higher than single junction solar cell maximum PCE 33.7%. The optimum band gap $E_g = 1.87$eV is higher than $E_g = 1.34$eV to collect more energy in the red region.

up converter is added to the solar cell. Similar to the down converter, the additional photocurrent also increases photocurrent extraction. In figure 3-4b, the up conversion solar cell PCE limit is plotted. The maximum PCE for an up conversion solar cell is 50.8%.

Enhancing Efficiency with Down Conversion + Up Conversion

In figure 3-5, the PCE limit of different energy conversion solar cell is compared. The up conversion solar cell has higher maximum PCE than a down conversion solar cell. The reason is that the high energy band gap solar cell has relatively less extraction loss. The performance of combined down+up conversion solar cells are also calculated, and as expected, they have an even higher maximum PCE of 51.2% [21]. Theoretically, such energy conversions may improve solar cell PCE. Finding and demonstrating efficient energy conversion would be important to realize PCE improvement. In the next section, I will discuss singlet fission and triplet-triplet annihilation, which are pathways to energy down and up conversion.

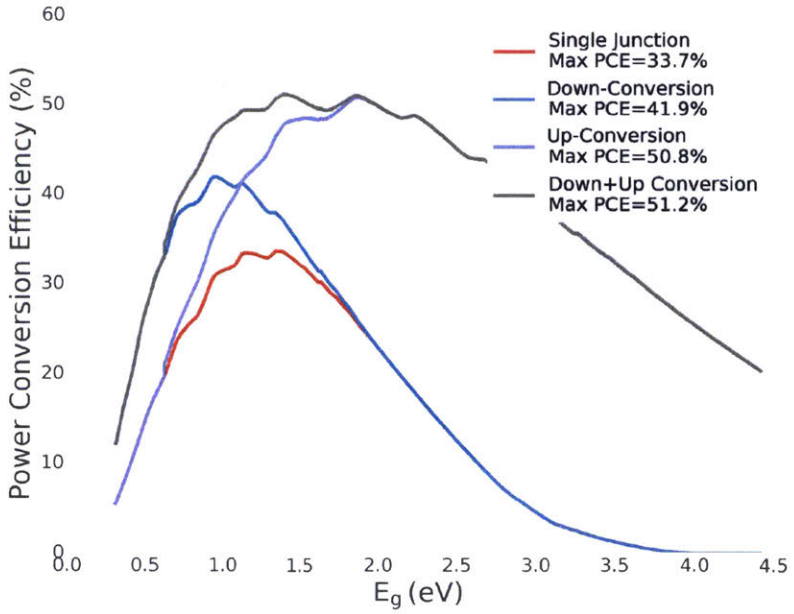

Figure 3-5: PCE Limit of Using Different Energy Conversion Schemes. The PCE limit with down+up conversion is plotted with down conversion, up conversion and a single junction solar cell. As expected, utilizing both down and up conversion increases the maximum PCE (51.2%).

3.2 Physics of Singlet Fission and Triplet-Triplet Annihilation

3.2.1 Singlet Fission

In this thesis, singlet fission [13? , 14? ? ?] is the down conversion mechanism studied. The basics of the singlet fission process is shown in diagram 3-6. When the triplet state energy E_T is about half of the singlet state energy E_S, singlet excitons in organic materials may undergo fission which splits them into two triplet excitons. The singlet exciton first transition into a triplet-triplet (TT) pair state [13]. The TT pair state can then dissociate into two triplet excitons, effectively doing energy down conversion. This process can be efficient because direct transition from singlet to triplets are not allowed or very inefficient based on selection rule 2.16. However, the TT pair state is a two particle system with a mixture of 9 possible states. Among the TT pair states, there are some that have singlet characteristics. This allows

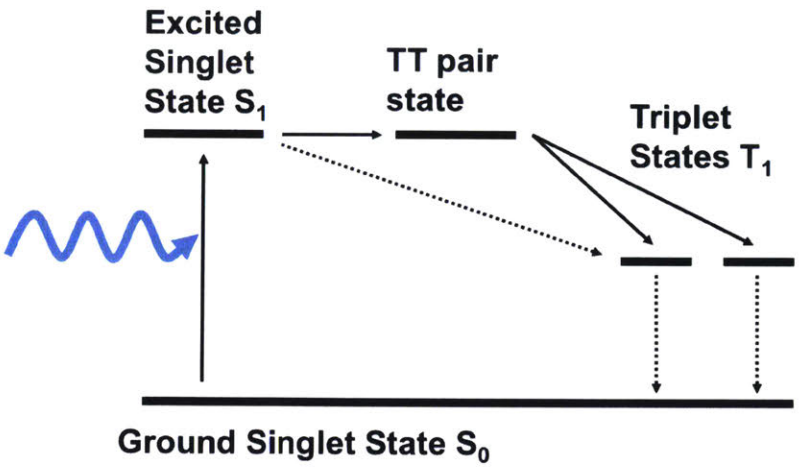

Figure 3-6: Schematic of Singlet Fission. When the triplet state energy E_T is about half of the singlet state energy E_S, singlet excitons in organic material may undergo fission which splits them into two triplet excitons. Singlet exciton first transition into a triplet-triplet (TT) pair state. The TT pair state can then dissociate into two triplet excitons, effectively doing energy down conversion. This process can be efficient because the direct transition from singlet to triplet is not allowed or very inefficient based on selection rule 2.16.

the transition from singlet states to TT pair states. Therefore, singlet fission is an attractive candidate for down conversion compared to other multi-exciton generations.

3.2.2 Triplet-Triplet Annihilation

Triplet-triplet annihilation (TTA) [12, 5] is the opposite process to singlet fission. Two triplet excitons merge and create a singlet exciton. The TT pair states once again serve the role of allowing the transition between two triplet states and a singlet state. In studies [26, 27], the authors have measured an intensity oscillation in the transient photoluminescence of singlet fission materials. This "quantum beating" shows the correlation between the two triplet spins m_s affects the generation of singlet excitons.

Merging two low energy triplet excitons ($2E_T \sim E_S$) and creating a high energy singlet exciton that could then be collected is a mechanism for energy up conversion. Triplet excitons are dark states which have longer lifetimes, allowing the triplet excitons to have enough time to diffuse and merge.

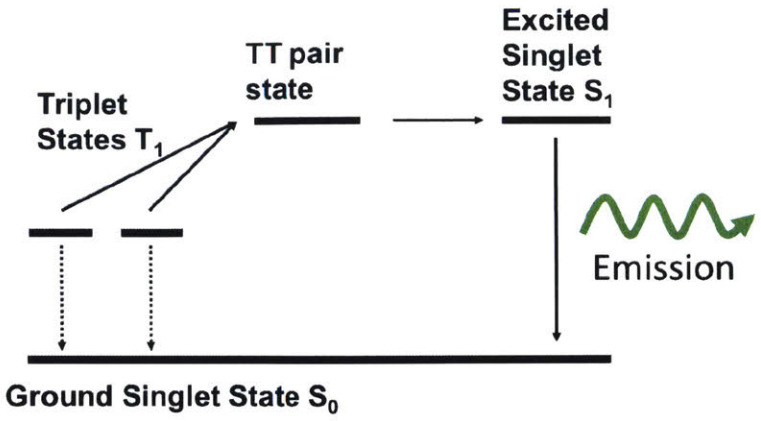

Figure 3-7: Schematic of Triplet-triplet Annihilation. Triplet-triplet annihilation (TTA) is the reverse process of singlet fission ($2E_T \sim E_S$). Two triplet excitons may diffuse and collide, forming a TT pair state. The TT pair state could then transition into a singlet exciton, which can then be collected through emission or charge-transfer states. TTA is a mechanism that does energy up conversion.

3.2.3 Magnetic Field Effect

Due to selection rule 2.16, singlet fission and triplet-triplet annihilation rate are determined by the numbers of TT pair states that have singlet characteristics. The external magnetic field affects how the singlet state is distributed in the TT pair states.

The singlet fission dependence on magnetic field can be explained with a simple kinetic model on the TT pair states. The following explanation is based on the paper from Merrifield [5]. The simple kinetic model of the exciton states is,

$$S_1 \underset{k_{-1}}{\overset{k_1}{\rightleftarrows}} (TT)^l \underset{k_{-2}}{\overset{k_2}{\rightleftarrows}} T_1 + T_1 \tag{3.1}$$

where k_x are the forward and k_{-x} are the backward rates of the model. S_1 is the excited singlet state; $(TT)^l$ is the triplet-triplet pair states; and T_1 is the independent triplet state. The l superscript denotes the 9 possible states for TT pair states. The $(TT)^l$ pair states are the eigenstates of the spin Hamiltonian,

$$H = g\beta \mathbf{B} \cdot (\mathbf{S_1} + \mathbf{S_2}) + D(S_{z_1}^2 + S_{z_2}^2) + E(S_{x_1}^2 + S_{x_2}^2 - S_{y_1}^2 - S_{y_2}^2) \tag{3.2}$$

where g is the g-factor, β is the Bohr magneton, $\mathbf{B}$ is the magnetic field, Ss are the spin operators and D, E are the zero field splitting paramters. In the equation, the first term represents the Zeeman interaction with applied magnetic field $\mathbf{B}$ and the remaining terms are the zero-field splitting of the triplets [5, 28].

Singlet Fission MFE

To simplify the dynamics in equation 3.1, the singlet fission rate k_{fis} is the total forward rate,

$$S_1 \underset{k_{-1}}{\overset{k_1}{\rightleftarrows}} (TT)^l \overset{k_2}{\rightarrow} T_1 + T_1 \tag{3.3}$$

$$S_1 \overset{k_{fis}}{\rightarrow} T_1 + T_1 \tag{3.4}$$

where we assume that the fusion of the separated triplet excitons is negligible due to their low concentration or the possible existence of an endothermic process from two triplets to one singlet exciton. For a simplified version of the exciton dynamics, the rate equation of the TT pair states could be expressed as,

$$\frac{d[(TT)^l]}{dt} = k_1 \left|\langle S_1|(TT)^l\rangle\right|^2 [S_1] - k_{-1} \left|\langle S_1|(TT)^l\rangle\right|^2 [(TT)^l] - k_2[(TT)^l]. \tag{3.5}$$

The inner product between the singlet and TT pair state $\langle S_1|(TT)^l\rangle$ is the singlet exciton component of each $(TT)^l$ state. $\langle S_1|(TT)^l\rangle = S_{0l}$ affects the transition rates between the states. S_{0l} are calculated from diagonalizing $(TT)^l$ for the Hamiltonian in 3.2, which is affected by magnetic field $\mathbf{B}$. Under steady state conditions, $\frac{d[(TT)^l]}{dt} = 0$ and at steady state $[S_1] = N_s$ (assuming with singlet generation). The $(TT)^l$ population is then,

$$[(TT)^l] = N_s \frac{k_1 |S_{0l}|^2}{k_{-1}|S_{0l}|^2 + k_2}. \tag{3.6}$$

From this, we can obtain the fission rate k_{fis} from $[(TT)^l]$,

$$k_{fis} = \frac{k_2 \sum_l [(TT)^l]}{N_s} = k_1 \sum_l \frac{|S_{0l}|^2}{\frac{k_{-1}}{k_2}|S_{0l}|^2 + 1} \tag{3.7}$$

where it depends on S_{0l}, which are affected by magnetic field. This exciton dynamics model does not consider coupling between the states within $(TT)^l$.A more complex model is described in [5, 28], however the difference in the MFE between the two models is not significant for out purpose, thus we will be discussing the trend in the MFE with the simple model.

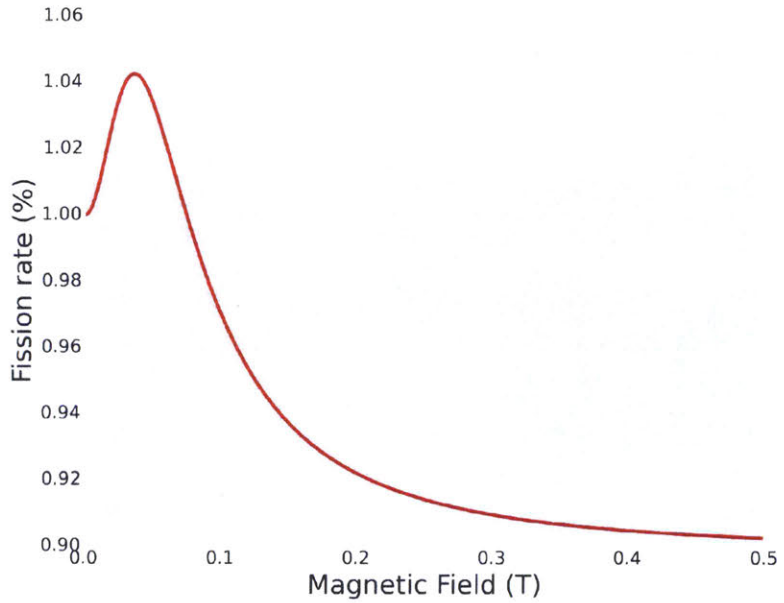

Figure 3-8: Magnetic Field Effect of Singlet Fission Rate from Equation 3.7. The fission rate first increases due to more TT pair states (from 3 up to 6) with spin 0 characteristics. It then decreased to 2 states with spin 0 characteristics, slowing the fission rate. The constants $D = -56 \pm 10$Oe and $E = 350 \pm 30$Oe used in equation 3.2 is from [5].

In figure 3-8, the magnetic field effect of k_{fis} are plotted. The modeling constants are from Merrifield et al [5], which is calculated for the MFE of anthracene. The fission rate k_{fis} has a distinctive dependency on applied magnetic field where the fission rate first increases and then decreases at large magnetic fields. The MFE of singlet fission is useful for identifying whether the measurement signals are triplet or singlet excitons. The triplet population MFE in singlet fission material should follow

the fission rate where the singlet population MFE is opposite; see figure 3-9.

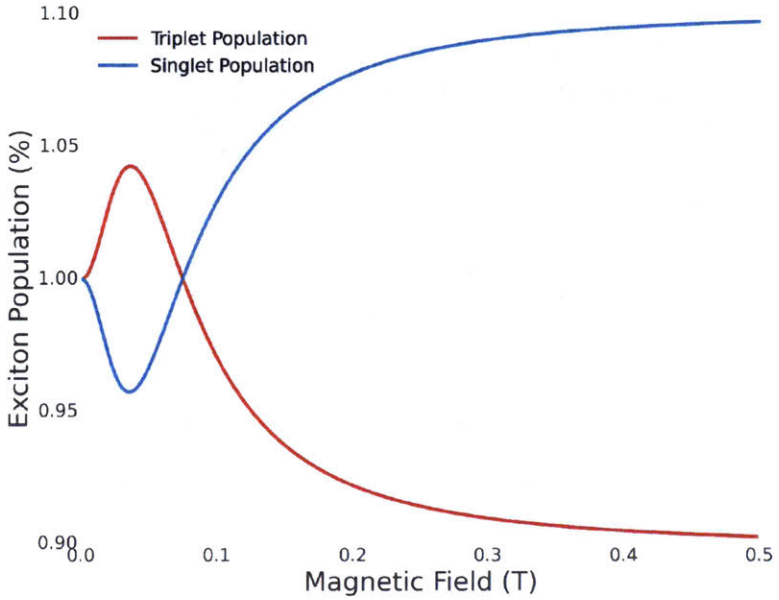

Figure 3-9: Singlet and Triplet Exciton Population under Magnetic Field in a Singlet Fission Material. The triplet population MFE in a fission material follows the fission rate because slower fission rates result in less triplet excitons. The singlet population MFE is opposite where a slower fission rate result in more singlet excitons.

Triplet-Triplet Annihilation MFE

For triplet-triplet annihilation rate, the total backward rate can be described as

$$S_1 \overset{k_{-1}}{\leftarrow} (TT)^l \underset{k_{-2}}{\overset{k_2}{\rightleftarrows}} T_1 + T_1 \tag{3.8}$$

$$S_1 \overset{k_{tta}}{\leftarrow} T_1 + T_1 \tag{3.9}$$

where singlet fission is assumed to be negligible due to an endothermic process from one singlet to two triplets. Similar to equation 3.5, the $(TT)^l$ rate equation and the steady state population are

$$\frac{d[(TT)^l]}{dt} = -k_{-1}|S_{0l}|^2[(TT)^l] - k_2[(TT)^l] + \frac{1}{9}k_{-2}[T_1]^2 = 0 \tag{3.10}$$

$$\Rightarrow [(TT)^l] = \frac{1}{9}\frac{k_{-2}[T_1]^2}{k_{-1}|S_{0l}|^2 + k_2}. \tag{3.11}$$

The TTA rate k_{tta} is then calculated as,

$$k_{tta} = \frac{\sum_l k_{-1}|S_{0l}|^2[(TT)^l]}{[T_1]^2} = [(TT)^l] = \frac{k_{-2}k_1}{9k_2}\frac{|S_{0l}|^2}{\frac{k_{-1}}{k_2}|S_{0l}|^2 + 1}. \tag{3.12}$$

From the equation, the k_{tta} have the same magnetic field effect as singlet fission. From intuition, this is correct since $|S_{0l}|^2$ affects how well singlet exciton and the two triplet excitons are coupled. Thus, reducing the factor $|S_{0l}|^2$ decreases the transition rates between the excitons. In TTA, the population MFE would be opposite to figure 3-9.

3.3 Applications with Singlet Fission and Triplet-triplet Annihilation

3.3.1 Available SF and TTA Materials

Triplet-triplet annihilation was first used to describe the photophysics in anthracene [29]. During late 1960s and early 1970s, Merrifield et al. devised the magnetic field effect model that explains triplet-triplet annihilation in anthracene [12, 5] and described singlet fission in tetracene [13, 30].

Singlet fission and triplet triplet annihilation gained interest as mechanisms to improve solar cell efficiencies [31, 32]. Over the years, singlet fission and TTA were found and measured in different organic molecules. Most molecules that exhibit the phenomena are oligoacenes (such as tetracene or pentacene and their derivatives); see figure 3-10. Another set of molecules are cartenoids which have bi-phenyl rings with carbon chains in between, though the study of singlet fission in these molecules are relatively new [14, 33, 34]. Other molecular structures with singlet fission usually still consist of multiple phenyl rings or conjugated carbon chains [35, 14].

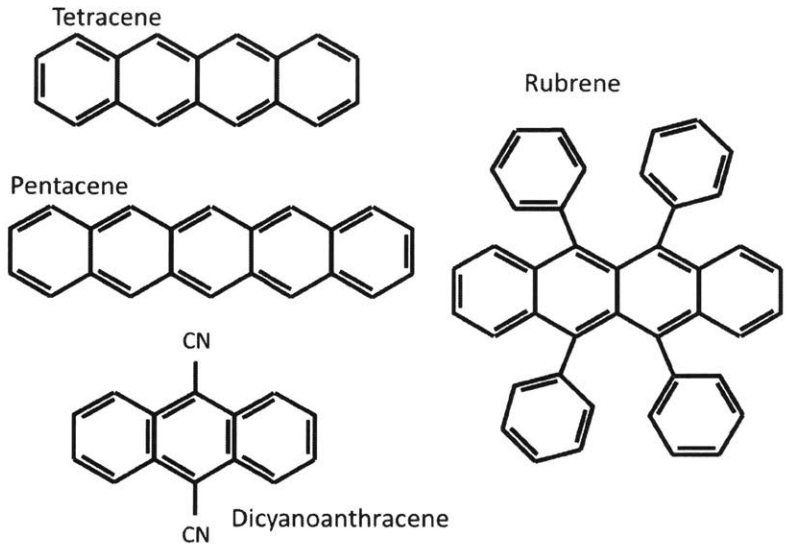

Figure 3-10: Common Singlet Fission and Triplet-Triplet Annihilation Molecules. Left, the top two molecules are tetracene and pentacene, oligoacenes with 4 and 5 phenyl rings. These two are well studied and have good singlet fission efficiencies. The bottom left molecule is 9,10-dicyanoanthracene, an efficient blue fluorescence emitter with triplet-triplet annihilation. The molecule on the right is rubrene, which is a tetracene derivative that also does TTA.

3.3.2 Singlet Fission OPV

As described above, singlet fission is interesting as a possible mechanism for energy down conversion in solar energy collections.

In 2011, Jadhav et al. [36] demonstrated a singlet fission solar cell that combined a singlet fission material that does high energy photon down conversion with a lower energy photon absorber. The paper used tetracene as the fission material and CuPC for the low energy photon absorber. The singlet fission efficiency of tetracene was 71%. This paper is one of the first step towards utilizing singlet fission in a down conversion solar cell.

To utilize singlet fission as a energy down converter in a solar cell, the efficiency of singlet fission is an important aspect. It is crucial for the singlet fission materials to be efficient (>100%) in terms of internal quantum efficiencies (IQE) or external quantum efficiencies (EQE). In 2013, Congreve et al. demonstrated a singlet fission OPV using pentacene with an IQE of 160% [6]. With optical trapping, they were

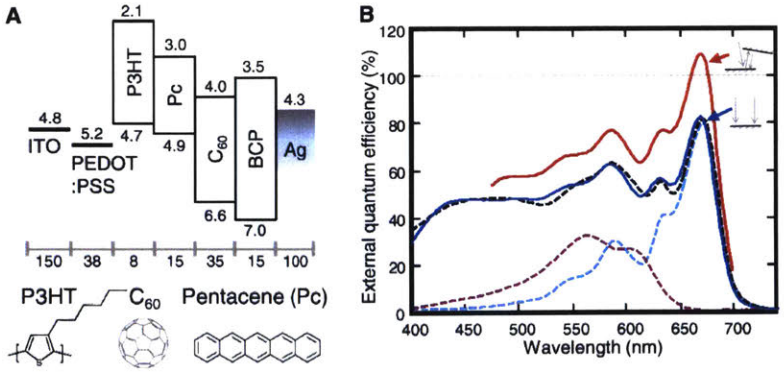

Figure 3-11: Device Architecture of Pentacene OPV and over 100% EQE. (result from [6], consent from authors.) (A) Chemical structures and architecture of the pentacene solar cell with the thickness of each layer in nanometers and energy levels of the LUMO and HOMO. (B) Over 100% external quantum efficiency of devices measured with light incident at 10° from normal with an external mirror reflecting the residual pump light (red line).

able to achieve over 109% EQE in pentacene OPV, which the EQE of the device is shown in figure 3-11. This is an important milestone, demonstrating the potential for using singlet fission material to increase solar cell efficiency.

In chapter 4 and 6, I will be focusing on both determining the singlet fission efficiencies in tetracene and demonstrating a possible structure for utilizing tetracene as the down converter for silicon solar cells.

3.3.3 Optical Up Conversion

An optical up conversion system which absorbs low energy photons and emits high energy photons could be useful in various applications, such as increasing solar cell efficiencies or infrared detection applications in biosensing and night vision. Optical up conversion can be very efficient in phase-matched nonlinear materials, pumped by high intensity coherent beams [37]. However for many of the applications mentioned, they require optical up conversion in low intensity, incoherent light. Thus, triplet-triplet annihilation became a possible candidate for the core of optical up conversion where triplet excitons generally have long transient lifetimes in organics.

In 2005, Islangulov et al. demonstrated low intensity up conversion by using metal-

to-ligand charge transfer and triplet-triplet annihilation materials [32]. In solution, it showed visible blue fluorescence from a 5mW 532nm laser excitation without focus.

Since optical up conversion applications is mainly interested in infrared sources, there has been research that extends the absorption wavelength of the optical up conversion system into infrared region. In Wu et al. 2016, they demonstrated absorption wavelength beyond 1μm with emission of 612nm, while also achieving a maximum of 1.2% of up conversion yield in this system [38].

In chapter 5, I will demonstrate a novel optical up conversion system that does not require heavy metals but enables a fully solid state process.

Chapter 4

Efficient Singlet Fission in Tetracene

4.1 Introduction

In this thesis, I will focus on utilizing tetracene as the down conversion material. As discussed in previous sections 3.1.2 and 3.2.1, when paired with a suitable low energy gap materials, singlet fission (down conversion) increases the power efficiency by reducing the thermalization loss through collecting extra photocurrent in the high energy photon region of the solar spectrum [21, 1]. Pentacene has shown efficient singlet fission with an IQE of 160% and 109% of peak EQE in an organic solar cell. However, the triplet exciton energy of tetracene is $E_T = 1.25$ eV [39] whereas the pentacene triplet energy is $E_T = 0.86$ eV [40, 41]. This makes tetracene a more suitable down converter for using silicon ($E_g = 1.12$eV) as the low energy gap material.

Tetracene is the most efficient fission material identified that can partner with the silicon, the predominant material of modern solar cells. Energy conservation during exciton fission requires that the initial exciton has approximately twice the energy of the product states. In tetracene, the fission process is thought to be slightly endothermic, resulting in a significant reduction in fission rate [39]. Nevertheless, the yield of triplet excitons is aided by spin conservation, which eliminates a thermalization loss pathway [6]. Due to the selection rule introduced in section 2.3.2, a singlet exciton with total spin S = 0 cannot rapidly decay directly into one lower-energy triplet exciton with total spin S = 1. Only the generation of two triplets is allowed

[14, 17, 42, 8]. Thus, singlet exciton fission in neat films of tetracene competes only with the relatively slow processes of singlet exciton fluorescence and non-radiative decay to the ground state. Indeed, multiple studies have shown or suggested a near unity efficiency for the fission process in neat films of tetracene [43, 44].

In this chapter, I will determine the efficiency for singlet fission in tetracene. The work is mainly published in Applied Physics letter, 2014 [45].

4.2 Device Structures and Fabrication

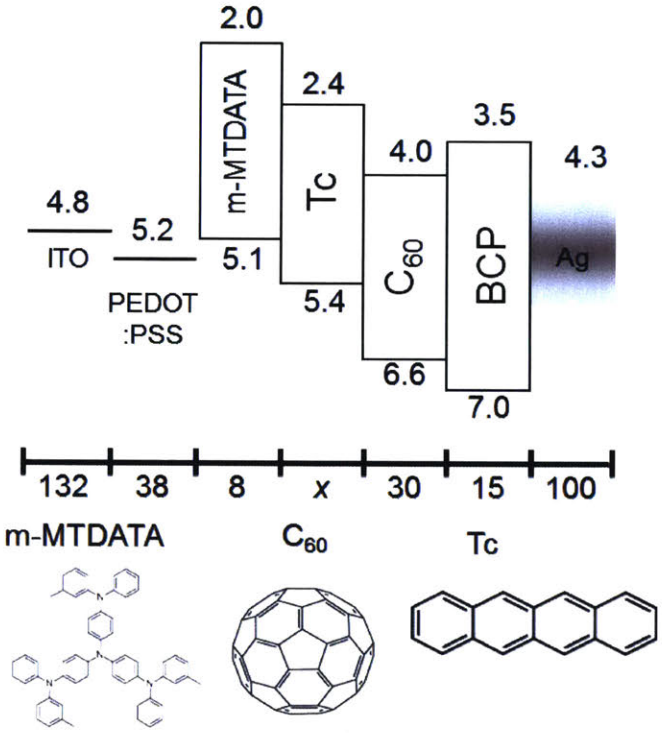

Figure 4-1: Device Structure and Band Diagram of Tetracene Photovoltaics and Photodetectors. For photodetector structures, tetracene/C_{60} layers are fabricated in multiple pairs of layers. Thicknesses are in nanometers and band energy levels are in electron volts. m-MTDATA is introduced as a triplet exciton blocking layer to increase exciton dissociation at the donor/acceptor interface. The structures of the molecules are also shown for m-MTDATA, tetracene and C_{60}.

In this work, there are two types of measurements that help us determine the fission efficiencies: photocurrent and fluorescence. The photocurrent is measured in a

photovoltaic or photodetector with tetracene. The device structures used to generate photocurrent and the energy levels of the constituent materials are shown in figure 4-1 [6, 8]. The devices are made from a pre-patterned anode of indium tin oxide (ITO), on glass substrates. The ITO substrates are cleaned by first sonicating in a detergent (Micro-90, 2% in volume). After rinsing in deionized water, the ITO substrates are sonicated in acetone to remove any organics. The substrates are then boiled in isopropanol (IPA) to remove remaining acetone. Finally, they are treated with oxygen plasma for 5 minutes. The organic materials and cathode (aluminum) are thermally evaporated on top of the cleaned substrates in a vacuum chamber at a pressure of 2×10^{-6} torr. The devices are then packaged with a UV-cured epoxy under nitrogen to avoid oxygen and water degradation during measurements. For fluorescence measurements, the sample structures are simply organic fluorescence layers (tetracene with or without C_{60}) thermally deposited in a vacuum chamber. The samples are also packaged for protection.

For comparison, we build devices from tetracene and pentacene using C_{60} in both cases as an acceptor molecule. In pentacene, singlet fission is exothermic, thus significantly faster than in tetracene, allowing us to study the impact of the fission rate in devices [6]. To block exciton losses at the anode, an exciton blocking layer is placed beneath the singlet fission material [46]. Based on the energy levels of the materials, we selected m-MTDATA for tetracene and P3HT for pentacene [6]. Both blocking layers have triplet energies greater than the fission material and highest occupied molecular orbit (HOMO) levels appropriate for extracting holes from the fission materials.

4.3 Magnetic Field Effect of Singlet Fission in Tetracene

4.3.1 Magnetic Field Effect Measurement

First, we would like to qualitatively show singlet fission in tetracene by measuring the magnetic field effect (MFE) in fluorescence and photocurrent. The setup to measure

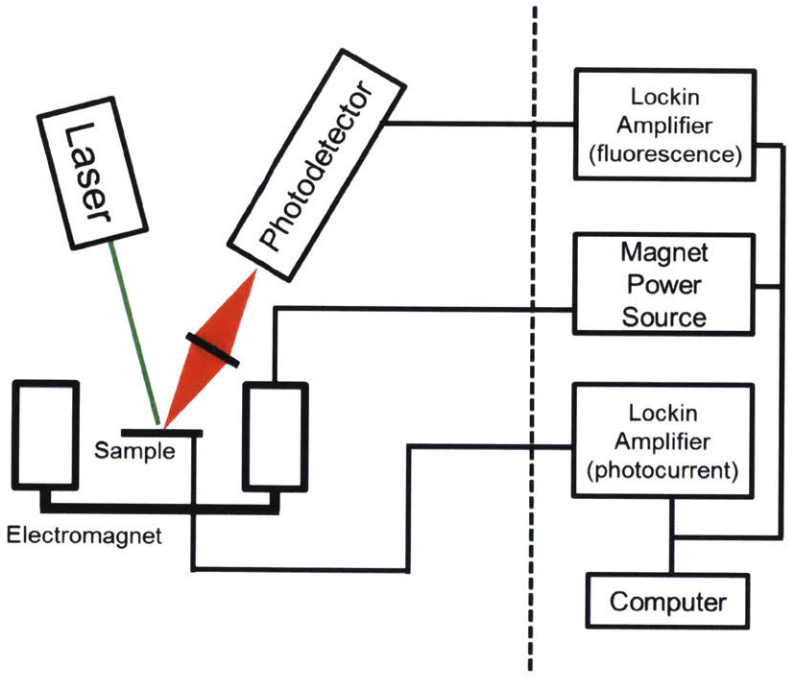

Figure 4-2: Magnetic Field Effect Measurement Setup. This is the setup to measure the magnetic field effect (MFE) of the fluorescence from tetracene film or photocurrent from tetracene device. To measure small signal changes under 0.1%, a lock-in amplifier (SR830) is used to measure fluorescence or photocurrent.

the MFE is shown in diagram 4-2. The samples are placed within an electromagnet, which can be controlled by an external power source. The excitation source is either a laser or LED. To measure the MFE of fluorescence from tetracene, we collect the emission and measure the signal by a photodetector with a lock-in amplifier. The photocurrent of the device is measured by the lock-in amplifier directly. In photodetector structures, a reverse biased voltage is applied to increase photocurrent collection.

The MFE in fluorescence or photocurrent could be on the order of 0.1%. To measure such small signal changes, we measure the fluorescence or photocurrent with alternating applied magnetic field from on to off for multiple cycles (usually 4 cycles, each cycle *sim* 45 seconds). With this measuring method, we can accurately pick up the small signal as well as correcting for sample degradation or excitation intensity drift. An example of the measured photocurrent (red curve) under 0.43T is plotted in figure 4-3. The device is 20nm of tetracene and 30nm C_{60} solar cell. To obtain the magnetic field effect change, the signals are fitted with a polynomial function of

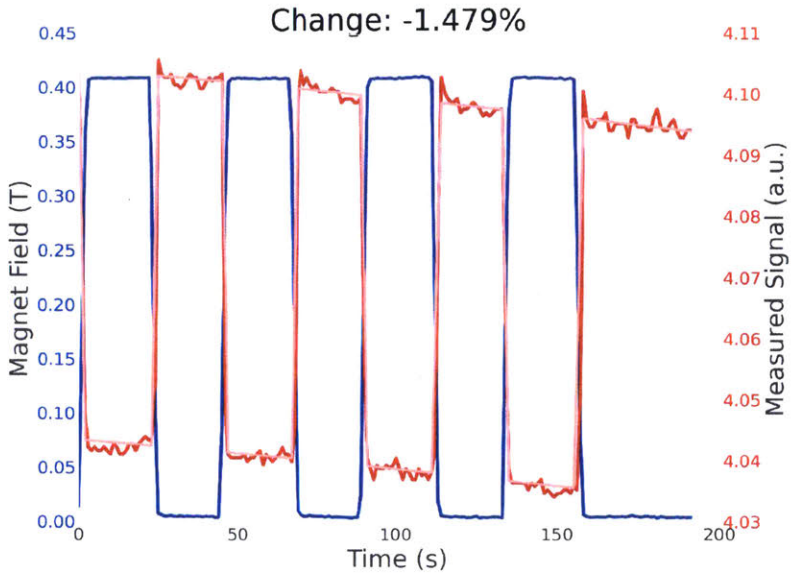

Figure 4-3: Magnetic Field Effect Analysis. To detect the small magnetic field effect changes, the external magnetic fields are applied in on to off cycles. This method allows us to reduce the effects of signal drift such as degradation or sample annealing. The signal curve (red) is fitted to a polynomial function of time $x(t)$ with a Δx change when magnetic field is applied (fitting curve: light red). Δx will be the magnetic field effect change. The magnetic field strength measured is plotted in blue. The measured signal is the photocurrent of a 20nm Tetracene/30nm C_{60} device.

time $x(t)$ with a Δx percentage increase in signal when magnetic field are applied. The calculated Δx will be the magnetic field effect change. In this example device, photocurrent changes -1.48% under magnetic field.

4.3.2 Magnetic Field Effect Measurement

With the MFE measurement setup and analysis in figures 4-2 4-3, we can measure the MFE in our tetracene samples, which are plotted in figure 4-4. The fluorescence MFEs are measured from tetracene crystals (green square) and thin film (red triangle). The photocurrent MFE is measured from a 30nm thick tetracene solar cell device, which displays opposite sign to the measured changes in fluorescence. Both fluorescence MFE trends matched well and follow the trend of singlet exciton population MFE; see figure 3-9. The photocurrent MFE matches to the triplet exciton population MFE. The results confirm that tetracene does singlet fission.

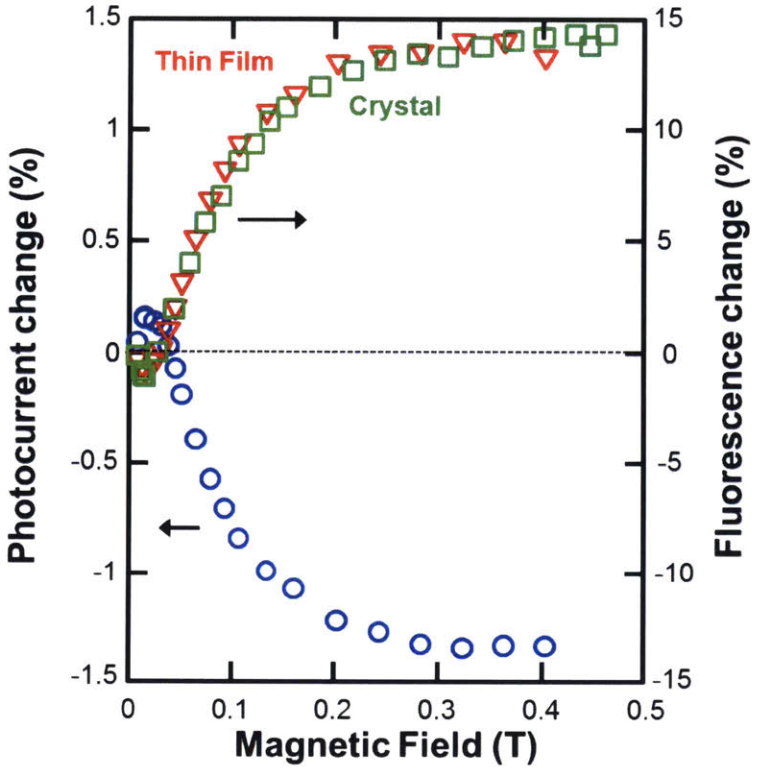

Figure 4-4: Magnetic Field Effect (MFE) of Tetracene. Fluorescence changes of tetracene crystals (green square) and thin film solar cells (red triangle) as a function of magnetic field. The photocurrent of a 30nm thick tetracene solar cell displays the opposite sign to the measured changes in fluorescence. Both fluorescence of MFE trends match well and follow the trend of the singlet exciton population. The photocurrent MFE matches to the triplet exciton populations.

4.4 Internal Quantum Efficiency

Singlet exciton fission in photovoltaic devices is complicated by the presence of additional important loss pathways such as singlet exciton dissociation into charges; see figure 4-5 [6, 47]. Consequently, it is typically insufficient to measure fission rates in neat thin films; practical applications require measurements of the triplet yield in devices. A lower limit is defined by the internal quantum yield (IQE) - the ratio of charges generated in the cell to photons absorbed for the specific layer. But determination of the IQE is especially challenging for tetracene devices, since its optical absorption overlaps with the usual acceptor material C_{60}. Alternative approaches for measuring triplet yield based on the temperature dependence of fission in tetracene

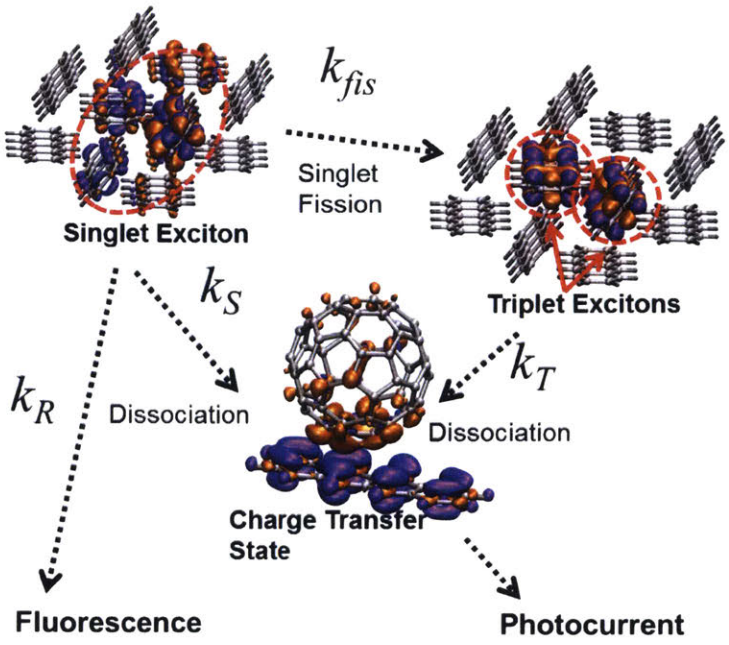

Figure 4-5: Modified Exciton Kinetic Model for Tetracene Devices. The modified kinetic model, compared to pentacene model in Congreve et al. [6], includes the fluorescence rate from singlet excitons.

[36] are also suspect given conflicting reports of the temperature dependence of the fission rate [43, 30] and the magnetic field effect in tetracene [48].

4.4.1 Optical Modeling

To accurately measure the IQE of tetracene, we first measure the solar cell's external quantum efficiency (EQE) under different wavelengths of incident light. To determine the IQE, we also need to obtain the optical n and k parameters of each of the materials [49]. Figure 4-6 is an example of estimating n and k from transmission and reflection. In Jadhav, et al. [36], it was shown that characterizing the absorption of tetracene layer is difficult due to scattering. The refractive index also changes under different tetracene thicknesses and materials it deposited on. For the n and k of tetracene used in this work, we determine the n and k parameters from transmission-reflection spectra with additional aid from absorption spectra [50, 7]. The n and k are determined for each individual tetracene thicknesses.

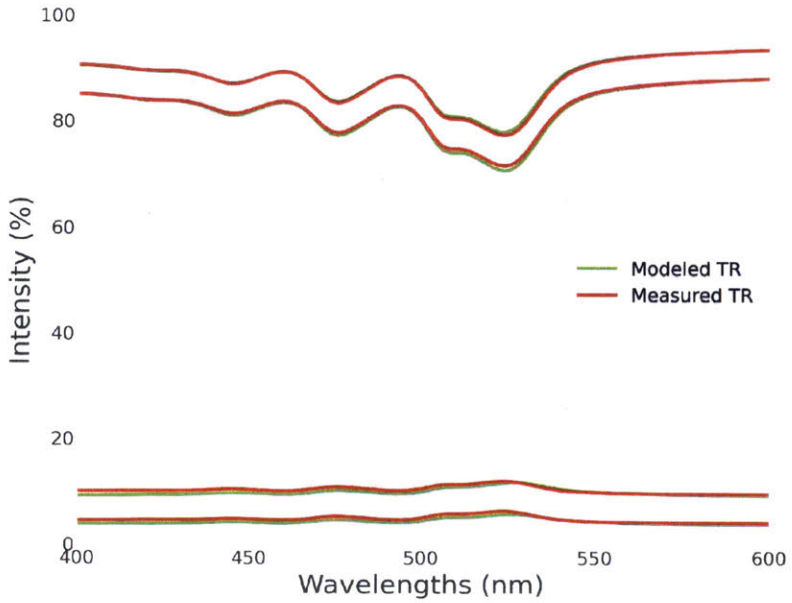

Figure 4-6: Measuring Refractive Index. The sample is a 15nm of tetracene on glass substrate. The transmission and reflectance (TR) of a sample are measured under excitation with traverse magnetic (TM) mode and traverse electric (TE) modes (green). With transfer matrix [7], the n and k of the material are then fitted to minimized the total errors (red).

With an optical transfer matrix [7], we can estimate each layer's absorption spectra, fitting the overall EQE by separately adjusting the respective IQEs of tetracene and C_{60}. The quality of the optical fit is assessed by comparing the measured photocurrent to the calculated absorption as a function of wavelength in figure 4-7. We find that the modeled photocurrent curve fits the experimental EQE data within a root mean squared error of 11%. Notably, there is a stronger $\lambda = 520$nm shoulder in the modeled curve that was not present in measured EQE.

4.4.2 Optimal Device and Efficiency

With the methods from above, we can optimize the tetracene solar cells or photodetectors to obtain the maximum IQE. The IQEs of the devices as well as the comparison pentacene devices are plotted in figure 4-8. The data show similar trends between two materials as a function of fission material thickness, but the overall photovoltaic performance is significantly worse in tetracene with a peak IQE of $127 \pm 18\%$ as com-

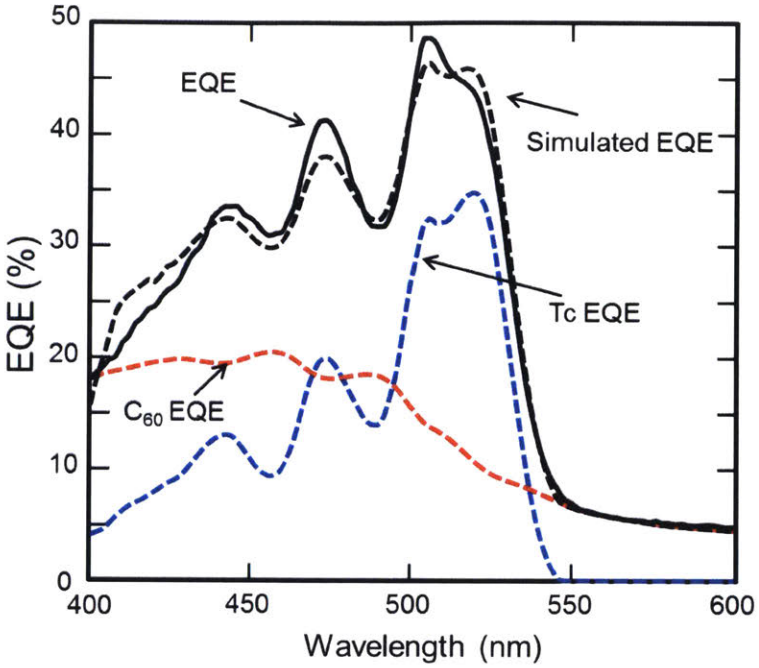

Figure 4-7: Obtaining Internal Quantum Efficiency of Devices. The dashed blue and red curves are estimated tetracene and C_{60} EQE contributions obtained by multiplying the absorption spectrum by a factor. The factor will be the IQE of the layer. The simulated photocurrent is a black dashed line and the measured EQE curve is a black solid line. The device is a photovoltaic cell with tetracene layer thickness x = 25nm.

pared to $160 \pm 10\%$ in pentacene. Tetracene exhibits a relatively slow fission rate [8] and hence it is less competitive with singlet exciton dissociation for thin tetracene layers. Consequently, the peak IQE in tetracene occurs for thicker layers where triplet diffusion losses are already significant. Nevertheless, the maximum IQE of tetracene is larger than 100%, making it feasible for a silicon solar cell down converter.

4.5 Triplet Exciton Yield

4.5.1 Exciton Dynamics in Tetracene Devices

To obtain the triplet yield in tetracene, we would need to determine the rates in figure 4-5. The magnetic field effects in figure 4-4 can provide a quantitative model of the yield of singlet exciton fission when they are combined with a kinetic model

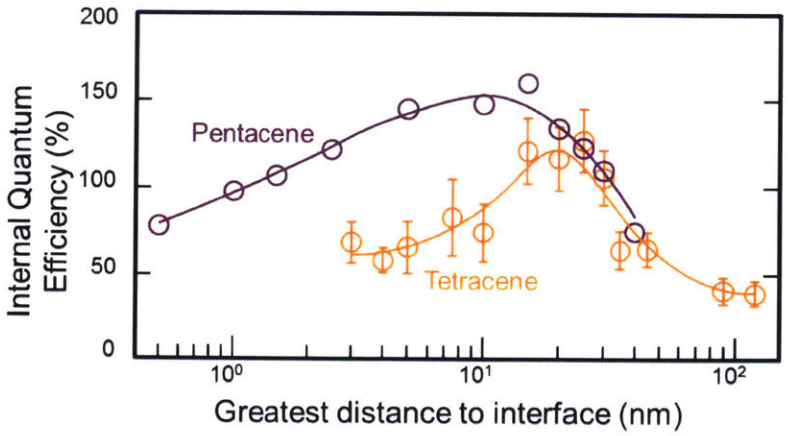

Figure 4-8: Internal Quantum Efficiency. The IQE of photovoltaic devices as a function of the thickness, x, of the constituent tetracene layer. From the data, a maximum IQE of $127 \pm 18\%$ is achieved in a tetracene device with $x = 25$nm. The pentacene data are compared (data from Congreve et al. [6]). The pentacene devices have a higher IQE of 160% and also show a faster fission rate with higher IQE in thin pentacene layers.

as described by 4-5. A photon is first absorbed by the fission material, creating a singlet exciton. The singlet exciton dynamics are affected by three rates: the radiative decay rate, k_R; the rate of singlet exciton dissociation into charge, k_S; and the effective singlet exciton fission rate, $k_{fis}(B)$. It is notable that charge generation occurs at donor-acceptor interfaces, so k_S can be tuned by adjusting the greatest exciton diffusion distance, d. Very thick tetracene layers have negligible singlet charge dissociation rates. Normalizing by the rate of fission under zero applied magnetic field, $k_{fis}(0) = k^0_{fis}$, we define $k_{fis}(B) = \chi_{fis}(B)k^0_{fis}$, $k_S(d) = \chi_S(d)k^0_{fis}$ and $k_R = \chi_R k^0_{fis}$.

The magnetic field-induced modulation, $\delta_I(B,d)$, of photocurrent, I, as a function of magnetic field, B, and greatest exciton diffusion distance, d, is:

$$\delta_I(B,d) = \frac{I(B,d) - I(0,d)}{I(0,d)} = \frac{(\chi_{fis}(B) - 1)(\chi_S(d) + 2\chi_R)}{(\chi_S(d) + \chi_{fis}(B) + \chi_R)(\chi_S(d) + 2)} \tag{4.1}$$

Similarly, the magnetic field-induced modulation, $\delta_F(B,d)$, of fluorescence, F is:

$$\delta_F(B,d) = \frac{F(B,d) - F(0,d)}{F(0,d)} = \frac{1 - \chi_{fis}(B)}{\chi_S(d) + \chi_{fis}(B) + \chi_R} \tag{4.2}$$

For large magnetic fields $B > 0.4T$, the normalized fission rate $\chi_{fis}(B)$ converges to a constant value χ_{fis}^m. Under $B > 0.4T$, both $\delta_I(B,d)$ and $\delta_F(B,d)$ have a limiting case for $d \to \infty$ when $\chi_S \to 0$:

$$\delta_I(B > 0.4T, d \to \infty) = \frac{(\chi_{fis}^m - 1)\chi_R}{\chi_{fis}^m + \chi_R} \tag{4.3}$$

$$\delta_F(B > 0.4T, d \to \infty) = \frac{1 - \chi_{fis}^m}{\chi_{fis}^m + \chi_R} \tag{4.4}$$

The photocurrent change also has an additional minimum value at a particular value of χ_S and d:

$$\delta_I(B > 0.4T, d_{max}) = \frac{\chi_{fis}^m - 1}{\left(\sqrt{2(1-\chi_R)} + \sqrt{\chi_{fis}^m - \chi_R}\right)^2} \tag{4.5}$$

Any two of the three potential experimental measurements: $\delta_I(B > 0.4T, d \to \infty)$, $\delta_F(B > 0.4T, d \to \infty)$ or $\delta_I(B > 0.4T, d_{max})$ allow us to solve for χ_{fis}^m and χ_R and then obtain $\chi_S(d)$ by measuring $\delta_I(B > 0.4T, d)$ or $\delta_F(B > 0.4T, d)$. But both photocurrent modulation measurements are complicated by additional photocurrent generation from C_{60} at overlapping wavelengths, forcing us to also estimate the IQE of tetracene and C_{60}. Thus, obtaining the triplet yield from the magnetic field effect on photocurrent is hampered by the same problem that obstructs direct measurements of the IQE in tetracene. We can, however, correct a δ_I measurement at a tetracene thickness for which we expect the IQE to be the most accurate, in this case $\delta_I(B > 0.4T, d \to \infty)$, and then rely on the δ_F measurement to predict the yield at varying thickness. Alternatively, we can find an approximate solution from the δ_F measurement alone. We explore both approaches below.

4.5.2 Magnetic Field Effect Dependencies on Exciton Diffusion Distance

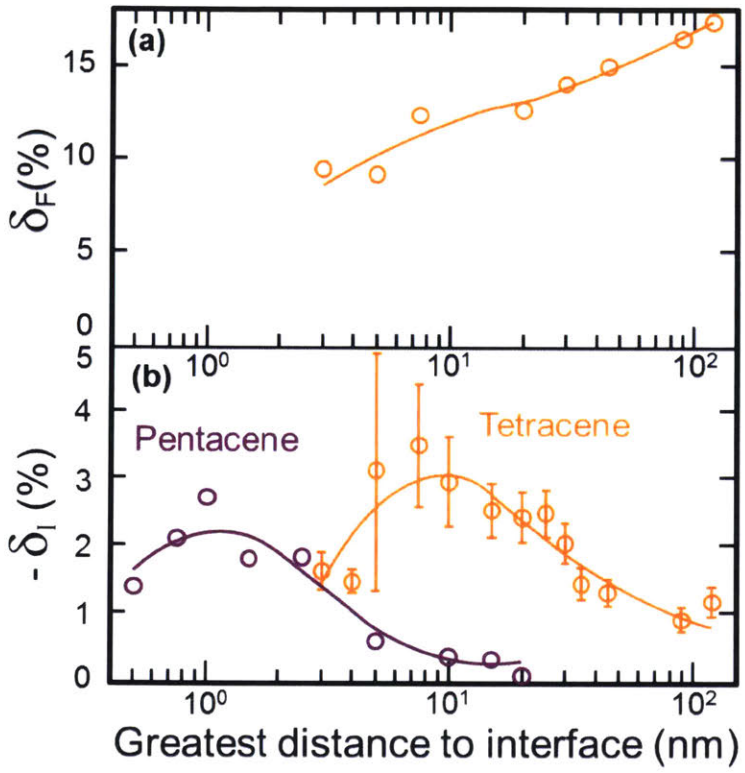

Figure 4-9: Magnetic Field Effects with Varying Exciton Diffusion Distance. The MFE of tetracene fluorescence change δ_F and photocurrent change δ_I are plotted as a function of the maximum exciton diffusion length in the device. The tetracene fluorescence MFE are measured in the corresponding sample with same thicknesses. The MFE of the photocurrent changes are corrected with the IQE ratio of tetracene and C_{60}. Pentacene δ_I are also plotted for comparison, showing again a faster fission rate.

In figure 4-9, the MFE of the tetracene fluorescence change δ_F and photocurrent change δ_I are plotted against the greatest exciton diffusion length in tetracene. This distance is the maximum length where all excitons created in tetracene would need to travel to reach the C_{60} interface. For a photovoltaic device, the distance is twice of the thickness of tetracene layer because of the blocking layer. In a photodetector device, the distance equals the thickness of tetracene layer. The tetracene fluorescence changes are measured in the corresponding device with same thicknesses. The MFE

of the photocurrent change are corrected with the IQE ratio of tetracene and C_{60}. The MFE trend of photocurrent follows expectations: the maximum modulation in observed at short diffusion lengths, decreasing at longer distances. Increasing the exciton diffusion distance allows the singlets to have time to change into triplet excitons, thus increasing MFE. However, very long distances allow all singlets to split into triplets, minimizing the rate change effect on triplet population. The pentacene δ_I is also plotted as comparison, again showing a faster fission rate.

4.5.3 Triplet Yield from Magnetic Field Effect

We can obtain the rates χ^m_{fis} and χ_R from the equations 4.3, 4.4 and the results measured in figure 4-9. For tetracene under strong magnetic fields of 0.4T, we find $\chi^m_{fis} = 84.5\%$ and $\chi_R = 5.07\%$.

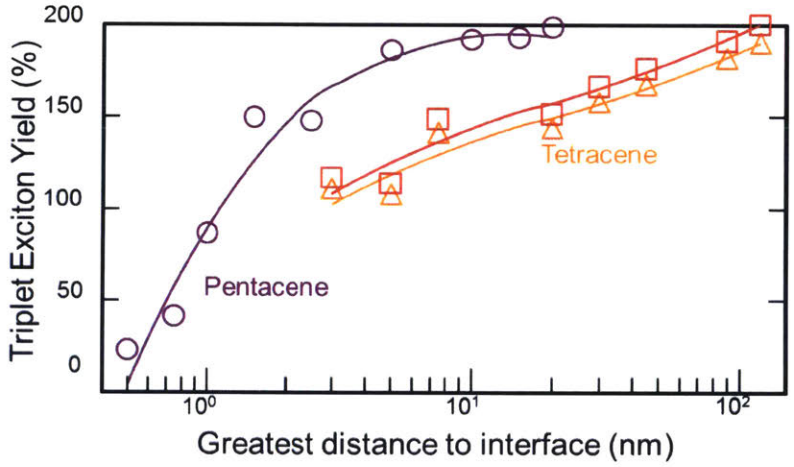

Figure 4-10: Triplet Exciton Yields in Tetracene and Pentacene. The red squares represent the triplet exciton yield approximated by the δ_F-only-approach. Orange triangles represent the full calculation of triplet yield based on both δ_F and the photocurrent change δ_I in figure 4-9. The data showed a maximum of 192% triplet yield in thick tetracene layers. As a comparison, pentacene reach 200% triplet yields.

From our measurement of fluorescence modulation under a magnetic field $\delta_F(B > 0.4T, d)$, we then calculate the normalized singlet loss rate $\chi_S(d)$ as a function of tetracene thickness, which allows us to determine the triplet yield: $2\chi^0_{fis}/(\chi_S + \chi^0_{fis} + \chi_R)$. The calculate triplet yield is plotted in figure 4-10. Recall that these values

are normalized by the zero field fission rate $\chi^0_{fis} =\sim 10ns^{-1}$ [51, 14, 44, 52]. The maximum triplet yield in a thick tetracene layer is 192%.

We also tested a δ_F-only-approach to estimating χ_S and triplet yield. For efficient singlet fission materials, the radiative loss rates, χ_R, are significantly smaller than χ_{fis}. Under this assumption we can simplify the magnetic field-induced modulation of fluorescence to

$$\delta_F(B > 0.4T, d) = \frac{1 - \chi_{fis}(B)}{\chi_S(d) + \chi_{fis}(B)}. \tag{4.6}$$

Solving at $\delta_F(B > 0.4T, d \to \infty)$, we find $\chi^m_{fis} = 85.2\%$. We then calculate $\chi_S(d)$ and the triplet exciton yield from $\delta_F(B > 0.4T, d \to \infty)$. In figure 4-10, we show that this estimate of the triplet exciton yield agrees well with the full model. The δ_F-only-approach requires a quenching interface, but does not require a device structure engineered to extract photocurrent or measurement of the IQE, while still producing a good estimation of χ^m_{fis}, χ_S and triplet yield. The accuracy of this approach could be further improved by including the ratio of fluorescence and fission rates as obtained from the photoluminescence transients in monomeric solutions and thin films.

From the triplet yield estimation, there are losses due to fluorescence in tetracene, which is notably stronger than pentacene but still weaker than other losses. Subtracting from the maximum possible efficiency of 200%, we estimate that 20% of the potential photocurrent in our best device is lost due to singlet exciton dissociation (collecting one charge per singlet exciton instead of two), 8% to fluorescence, and the remaining 45% due to triplet exciton diffusion, yielding the final IQE value of $127 \pm 18\%$.

4.5.4 Singlet Exciton Dissociation Rates

As an additional verification for the determination of triplet yield, in figure 4-11 we compare our estimates of the singlet loss rate to the ones of measured. As expected, the average rate of the extracted direct singlet exciton dissociation loss increases as

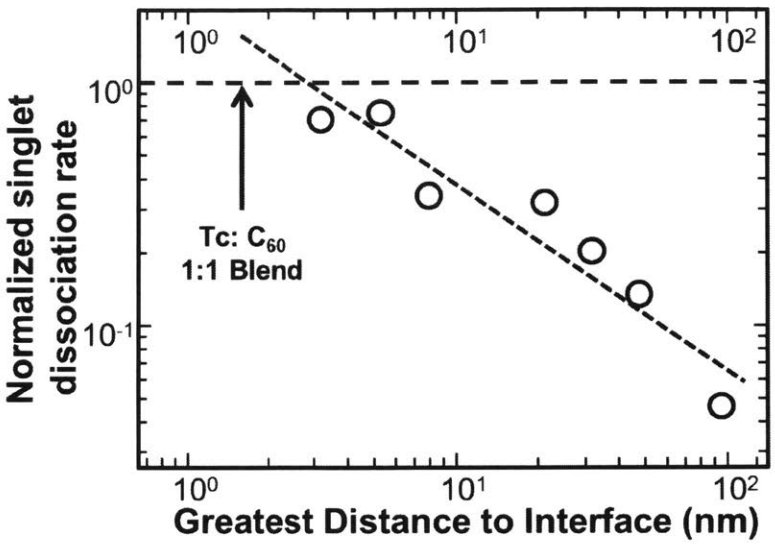

Figure 4-11: Singlet Dissociation Rates. Singlet dissociation rate χ_S from modeling fluorescence change plotted with different exciton traveling length. The χ_S of tetracene:C_{60} blend in Yost et al. [8] was included as a comparison with our method.

the tetracene layer thickness decreases. In our thinnest photodetector we determine $k_S = 0.8k^0_{fis}$, which is consistent with the measured rate of $k_S \sim k^0_{fis} \sim 8.3\text{nm}^{-1}$ for a tetracene-C_{60} blended thin film featured in figure 5a of Yost, et al. [8].

4.6 Conclusion on Tetracene

We find that the slow rate of singlet exciton fission in tetracene lowers its triplet yield within a 20 nm distance from a C_{60} interface. Pentacene exhibits faster exciton fission and higher yields at similar distances, highlighting the importance of designing exothermic rather than endothermic fission materials. Nevertheless, tetracene can yield internal quantum efficiencies that exceed 100%. In optimized organic solar cells we find a peak triplet yield of $153 \pm 5\%$ with an IQE of $127 \pm 18\%$. These results agree with prior work [36], although we find here that thicker layers of tetracene are required to optimally compete with singlet exciton dissociation. We have also demonstrated that the exciton yield in tetracene can be determined simply from the magnetic field modulation of fluorescence without measuring photocurrent or IQE.

Chapter 5

Metal-Free Solid-State Optical Up Conversion

5.1 Introduction

As mentioned in section 3.3.3, applications of optical up conversion are interested in converting infrared into visible light and requires low intensity to be practical. This makes triplet-triplet annihilation (TTA) an attractive mechanism for energy up conversion. The triplet exciton typically has a long lifetime since transitions between triplet states (total spin $S = 1$) and singlet ground states ($S = 0$) are spin disallowed due to selection rule (section 2.3.2). TTA can convert two triplets into a radiative singlet state. However, since transitions between the ground state an triplet excited states are disallowed, a triplet exciton sensitizer is required to absorb low energy photons and generate triplet excitons that can then Dexter transfer [1] to the TTA materials.

In most optical TTA up conversion systems, a heavy metal atom is often used to promote spin orbit coupling in the sensitizer, enhancing inter-system crossing and the generation of triplet excitons [32, 53, 54]. For most optical up conversion studies, the effect is demonstrated in solution or solution processed polymer films. The disadvantages for these systems include requiring heavy metal that could be more expensive and the requirement for solution processing that generally reduces the operation life-

time relative to thermally evaporated devices.

Here in this chapter, I will demonstrate an optical up conversion device structure that does not require heavy metal and are fabricated by thermal deposition. The work is mainly published in Applied Physics letter, 2016 [55].

5.2 Device Design

5.2.1 Thermally Activated Delayed Fluorescence

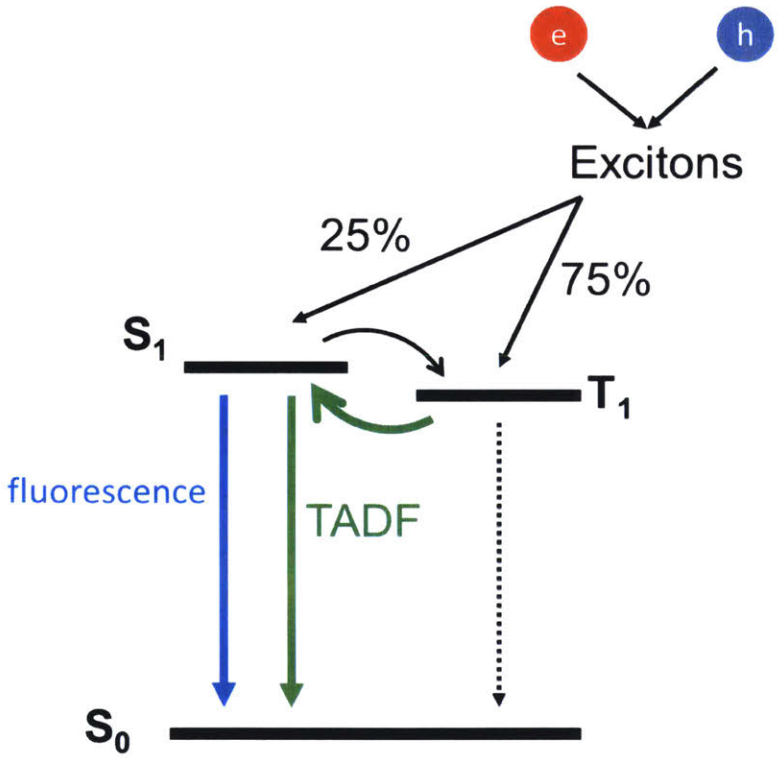

Figure 5-1: Schematic of Thermally Activated Delayed Fluorescence. In OLEDs, an exciton formed by electron and hole recombination creates 25% singlet excitons and 75% triplet excitons. In thermally activated delayed fluorescence (TADF), the energy gap between singlet and triplet state are designed to be small (< 0.1eV). This increases the thermally induced inter-system crossing from triplet excitons back to singlet excitons and then fluoresce.

To eliminate the need for heavy metals and solution processing, we require a triplet sensitizer without heavy metal. Here we use a set of organic molecules that

do thermally activated delayed fluorescence (TADF) [56], where the schematics are shown in figure 5-1. Normally, combined electron hole pairs create the excitons in a 1 to 3 ratio of singlets and triplets, due to the three m_s configurations for the triplet excitons. In OLED, phosphorescence molecules [57, 58] utilize heavy metals that allow triplet excitons to emit. In a TADF molecule, the singlet and triplet excitons energy differences are designed to be small ($\Delta E_{ST} < 100$ meV) such that the triplet excitons can thermally transition back to the singlet and fluoresce. Here we utilize TADF molecules, which can also efficiently generate triplet excitons at efficiencies up to 70%, as the triplet exciton sensitizers. More importantly, the smaller exchange splitting ΔE_{ST} yields a smaller Stokes shift, and therefore, wastes less energy than a phosphorescent sensitizer.

5.2.2 Structure and Fabrication

In figure 5-2, we demonstrate the use of a TADF sensitizer for an TTA optical up converter. We employ the red TADF molecule 4CzTPN-Ph first reported by Adachi and co-workers [56] with $T_1 = 2.21$eV. 4CzTPN-Ph is used to sensitize 9,10-diphenylanthracene (DPA) [32] with $T_1 = 1.77$eV, $S_1 = 3.06$eV. DPA is used for both TTA and as the emitter of the high energy photon due to its suitable exciton energy levels and efficient photoluminescence quantum yield. Devices are fabricated using vacuum thermal evaporation at a base pressure of approximately 10^{-6} Torr. 50-nm-thick and 20-nm-thick films of DPA and 4CzTPN-Ph, respectively, are deposited consecutively onto pre-cleaned quartz substrates. We also prepared separate films of DPA and 4CzTPN-Ph for control experiments. The devices are then encapsulated under a nitrogen environment to prevent degradation from oxygen and water contamination.

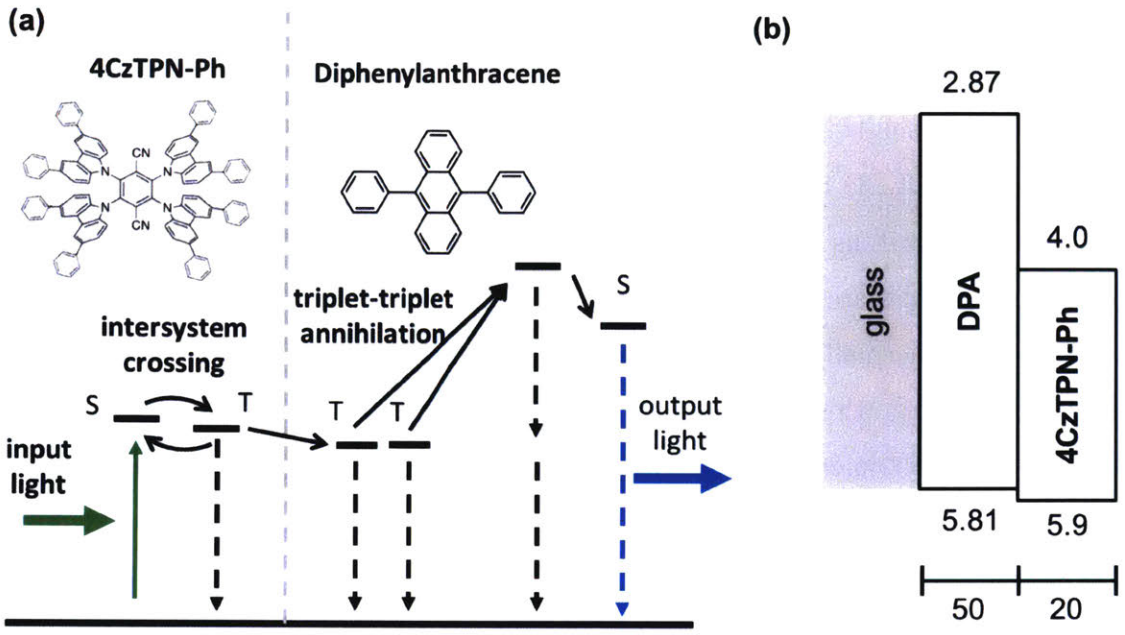

Figure 5-2: TADF-TTA Up Conversion Schematics and Device Structure. (a) The low energy excitation photons are first absorbed by the TADF molecule 4CzTPN-Ph, creating singlet excitons. Due to strong inter-system crossing in TADF, the singlet excitons form triplet excitons. A triplet exciton on 4CzTPN-Ph can then Dexter transfer to the triplet on DPA and up convert to a singlet exciton via triplet-triplet annihilation. High energy photons then emit from singlet excitons. (b) Our devices are simple bilayer thin films with 50nm of DPA and 20 nm of 4CzTPN-Ph. The HOMO and LUMO energies of DPA are 5.81eV and 2.87eV [9], where the energy levels of 4CzTPN-Ph are 5.9eV and 4.0eV [10].

5.3 Triplet-Triplet Annihilation Up Conversion

5.3.1 Up Conversion Emission Spectrum

To measure optical up conversion, we use a $\lambda = 532$ nm green laser with a maximum power of 400 mW. The TTA up converted emission is filtered through a $\lambda = 500$ nm short pass filter and measured in a spectrometer, yielding the emission spectrum shown in figure 5-3. Up converted light is absent in both single layer structures, but the bilayer DPA/4CzTPN-Ph thin film shows strong up conversion emission from $\lambda = 400$ nm to 500 nm. The emission peaks from $\lambda = 400$ nm to 475 nm are characteristic of DPA fluorescence. The prominent peak at $\lambda = 490$ nm is not observed in the fluorescent spectrum of neat DPA and is attributed to an exciplex of DPA and

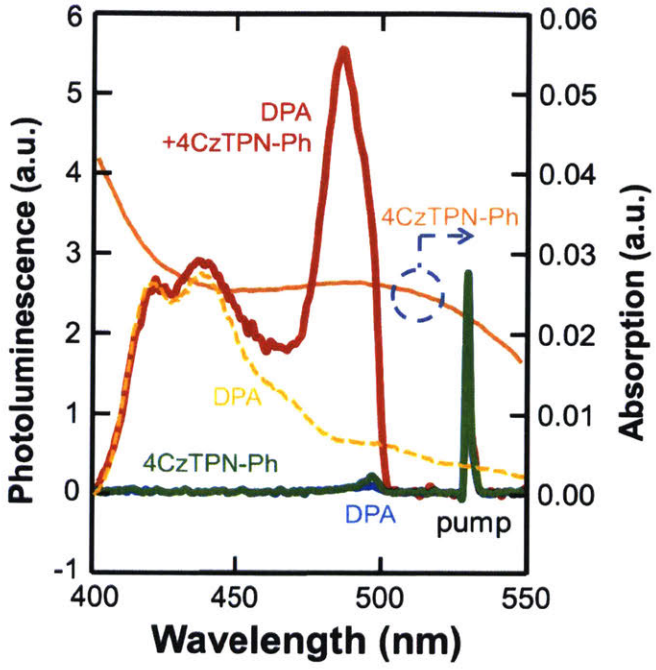

Figure 5-3: Optical Up Conversion Spectrum. The spectrum shows emission from three different devices (red, green, blue curve) with 532nm laser excitation. The red curve is DPA+4CzTPN-Ph device emission, where there are significant emission between 400nm - 500nm comparing to emission spectrum of 4CzTPN-Ph (green) and DPA (blue) only. This is attributed to up conversion emission. The yellow dotted curve shows the DPA fluorescence spectrum as a comparison.

4CzTPN-Ph. Indeed, we note the HOMO-LUMO offset at the DPA/4CzTPN-Ph interface suggests electron transfer from DPA to 4CzTPN-Ph and hole transfer from 4CzTPN-Ph to DPA; see (b) in figure 5-2. The absorption of 4CzTPN-Ph is observed to be broad and red-shifted as compared to DPA. The strong donor-acceptor character of the excited state in 4CzTPN-Ph, however, is associated with both weak exchange splitting and weak oscillator strength. As a consequence, the 20-nm-thick film of 4CzTPN-Ph absorbs just 6.8% of the incident pump light at $\lambda = 532$ nm. However, thicker films suffer from excessive losses due to poor exciton diffusion in organics.

5.3.2 Magnetic Field Effect of TTA Up Conversion

In figure 5-4, we confirm the presence of TTA up conversion by measuring the modulation of the DPA fluorescence under magnetic field. The MFE of the up converted

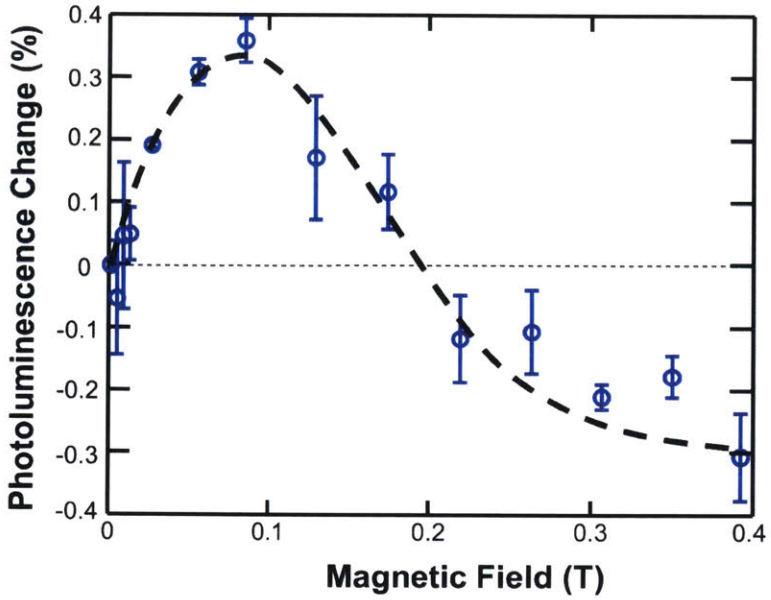

Figure 5-4: Up Conversion PL Change under Magnetic Field. The magnetic field effect shows up conversion rate correlates to triplet-triplet annihilation rate under magnetic field.

light is expected from the magnetic field model of Johnson and Merrifield [5], where the up converted photoluminescence increases under small magnetic field ($\sim$ 0.1 T) and decreases under strong magnetic field ($>$ 0.3 T). As a control experiment, no magnetic field effect is observed for 4CzTPN-Ph alone. This experiment confirms that our optical up conversion design utilizes TTA for energy up conversion.

5.4 Up Conversion Efficiencies

5.4.1 Up Conversion Quantum Yield

The quantum yield of up conversion (η_{UP}) of a system is the ratio of emitted short wavelength photons to absorbed long wavelength photons. Typically, the ratio is normalized to a maximum efficiency of 100%, [59] corresponding to two long wavelength photons combining to form a single short wavelength photon. We decompose the overall up conversion yield into: (i) efficiency of inter-system crossing, η_{ISC}, from singlet to triplet on the sensitizer; (ii) the Dexter transfer efficiency, η_{DEX}, of triplets

coupled from the sensitizer to the emitter; (iii) the TTA efficiency, η_{TTA}, for triplets up converting into singlets, (iv) "back transfer" losses, η_{BL}, caused by Förster energy transfer from the emitter back to the sensitizer, and (v) the fluorescent quantum yield of the emitter, η_{PL}. The overall up conversion efficiency can be written as,

$$\eta_{UP} = \eta_{ISC}\eta_{DEX}\eta_{TTA}\eta_{BL}\eta_{PL}. \tag{5.1}$$

However, it is difficult to measure the emission intensity of the up converted emissions in an integrating sphere due to the low photoluminescent quantum yield (PLQY). Instead, the relative up conversion efficiency is quantified by comparing the DPA emission excited by $\lambda = 365$ nm light-emitting diode (LED) and emission excited with the green laser $\lambda = 532$ nm. Both these excitation and measurements are done on the same bilayer sample of DPA | 4CzTPN-Ph. We measure the efficiencies on the exact same sample, spot location and fixed collection optics. The emissions for each excitations are,

$$PL_{365} = I_{365}A_{DPA}\eta_{PL}F \tag{5.2}$$

$$PL_{532} = I_{532}A_{4CzTPN-Ph}\eta_{ISC}\eta_{DEX}\eta_{TTA}\eta_{BL}\eta_{PL}F \tag{5.3}$$

where the geometric factor F is the collection efficiency for a given optical setup. I is the excitation intensity and A is the absorption for the specified layer, which is measurable. By dividing the two measured emissions, the relative up conversion quantum yield can be calculated,

$$\frac{\eta_{UP}}{\eta_{PL}} = \eta_{ISC}\eta_{DEX}\eta_{TTA}\eta_{BL} = \frac{PL_{532}I_{365}A_{DPA}}{PL_{365}I_{532}A_{4CzTPN-Ph}} \tag{5.4}$$

The relative up conversion yield is measured with $\eta_{UP}/\eta_{PL} = 1.1\%$. The efficiency is understood as the conversion yield of exciton pairs in the sensitizer into singlet

excitons in the annihilator. The PLQY of DPA in this structure can then be measured in a sphere with $\eta_{PL} = 25.2\%$, resulting a total up conversion efficiency of $\eta_{UP} = 0.28\%$. Scaling by the absorption yields an external quantum efficiency at $\lambda = 532$ nm of $\eta_{EQE} = 0.01\%$, demonstrating that substantial improvements in the device structure are still required. For example, future solid-state device structures should improve absorption using multi-layers, rough interfaces with large surface areas, or exothermic gradients to guide excitons to the sensitizer/annihilator interface.

5.4.2 Estimated Intensity for Up Conversion

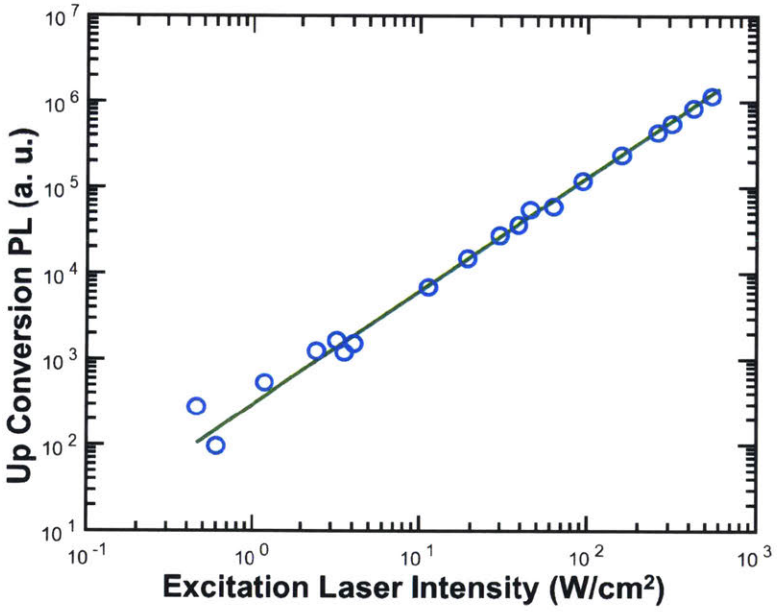

Figure 5-5: Relation Between Up Converted Photoluminescence and Excitation Intensity. We show the relationship with trend $PL \propto I^{1.28}$.

In figure 5-5, we measured the excitation intensity dependence of the upconversion photoluminescence. We model the trend as $PL = AI^x$. The data show $x = 1.28$ under regression. Following Kondakov, [60, 61] the near-linear intensity dependence can be understood from a simple model of the TTA kinetics. Assuming a triplet generation rate, G, in the DPA film, we can identify linear and quadratic processes

$$k_{decay}[T] + k_{up}[T]^2 = G. \tag{5.5}$$

The linear process k_{decay} represents geminate triplet losses in DPA, including non-radiative recombination to the ground state. The bimolecular process k_{up} represents the TTA process. If geminate triplet losses dominate the triplet dynamics, then we observe that the TTA process depends quadratically on G. But if TTA dominates, then upconversion exhibits a linear dependence on optical pump power [62]. The transition from quadratic to linear intensity dependence is, therefore, an indication of the minimum pump power required to realize efficient TTA [60, 61]. We cannot identify the quadratic-linear transition at low intensities in this system due to weak absorption in the thin sensitizer film and the low overall yield of upconversion. The power law exponent of 1.28 suggests, however, that some important non-geminate loss mechanism not considered in equation 5.5 remains even at high intensities. Possible candidates for this loss include triplet-singlet or triplet-triplet annihilation in the sensitizer, where delayed fluorescence is quenched by Förster transfer to neighboring singlet or triplet excited states [63]. Trap filling during diffusion could also affect the intensity dependence. Nevertheless, the minimum incident intensity of 0.5 W/cm^2 corresponds to approximately 30 W/cm^2 of absorbed power. This is consistent with prior work of Kondakov et al. showing that the high density of triplet excitons created in solid-state devices can exhibit high yields of up conversion at low excitation densities [61].

5.4.3 Triplet Sensitizing Rate

The losses in the up conversion process are probed further in figure 5-6, where we compare the transient delayed fluorescence of neat 4CzTPN-Ph to the transient delayed fluorescence of 4CzTPN-Ph in the bilayer DPA structure. The delayed fluorescence reports the triplet exciton lifetime in the 4CzTPN-Ph TADF dye, and hence allows us to extract η_{DEX} in this system. Based on delayed fluorescence lifetimes of 1.72 μs and

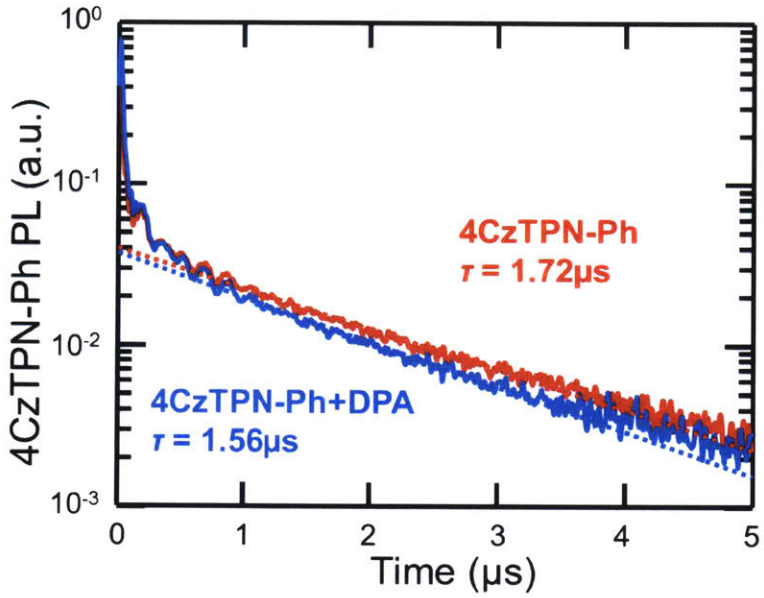

Figure 5-6: 4CzTPN-Ph Dexter Transfer to DPA. The red and blue curve represent the triplet delayed fluorescence rate of 4CzTPN-Ph. With DPA, the transient lifetime of 4CzTPN-Ph decreases from $1.72\mu s$ to $1.56\mu s$. The decrease is due to triplet exciton quenching with DPA. We show that the in our system, 9.1% of triplets in 4CzTPN-Ph are transferred to DPA.

1.56 μs in the neat film and bilayer structures, respectively, we obtain $\eta_{DEX} = 9.1\%$. The result is presumably limited by poor excited state diffusion in the 20-nm-thick 4CzTPN-Ph film. Improving triplet energy transfer is, consequently, a second attractive target after increasing the absorption for future generations of up conversion devices.

5.5 Conclusion

In this chapter, we demonstrate optical up conversion utilizing TADF molecules in a double layer film. Although the overall quantum yield of upconversion remains lower than prior work in solution using conventional sensitizers with high spin-orbit coupling, TADF materials as triplet exciton sensitizers are promising because their small splitting brings us closer to the ideal case of halving the wavelength during up conversion, and the absence of heavy metals such as Pd or Pt could lower the cost if

this technology becomes widespread. Thus, these results open the door to non-heavy metal sensitizer materials that show up conversion in solid state structures.

Chapter 6

Tetracene Triplet Excitons Transfer to Silicon

6.1 Introductions

In chapter 4, we have described our interest in studying tetracene as a potential down converter for silicon. The triplet exciton energy of tetracene is $E_T = 1.25$ eV [39], making it a suitable down converter material for silicon ($E_g = 1.12$eV) as the low energy gap material. In that chapter and the paper [45], tetracene was observed to exhibit a maximum IQE of $127 \pm 18\%$ in a device and a triplet yield of 192%. This work demonstrated that tetracene is a relatively efficient fission material with IQE $> 100\%$. Indeed the IQE in a well-designed combination with silicon should be larger than observed in the photovoltaics since in the sensitization, fission does not necessarily compete with the fast exciton dissociation at a donor acceptor junction.

To realize tetracene as down converter for silicon, we need to show triplet exciton transfer from tetracene to silicon. Figure 6-1 shows the basic schematics for photon absorption and exciton transfer. For photon energies $E_{hv} > 2.3$eV, the photons could be absorbed by tetracene and split into to lower energy triplet excitons $E_T = 1.25$eV. If the triplet excitons can transfer to silicon and be collected as charges, then effectively the down converter collects more photocurrent per absorbed photon in the blue. The silicon material by itself could still absorb photons from $E_{hv} = 1.12 \sim 2.3$eV.

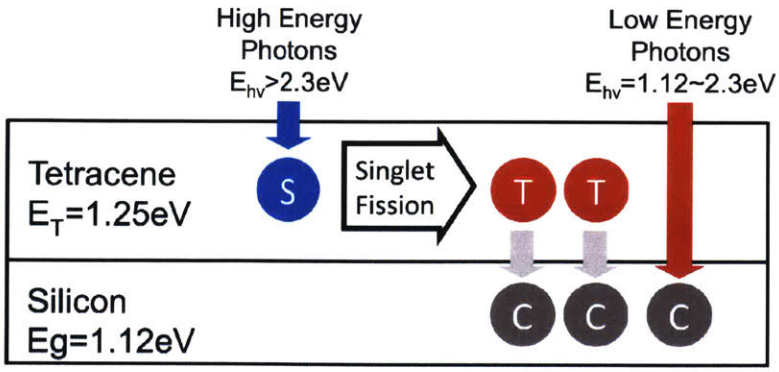

Figure 6-1: Schematics of Tetracene Down Converter for Silicon. For photon energy $E_{hv} > 2.3$eV, the photons are absorbed by tetracene and split into to lower energy triplet excitons $E_T = 1.25$eV. If the triplet excitons then transfer to silicon and are collected as charges, then effectively this down converter collects more photocurrent per absorbed photon in the blue. The silicon material by itself still absorb photons from $E_{hv} = 1.12 \sim 2.3$eV.

There have been some efforts prior to demonstrate a triplet exciton transfer from a singlet fission material to silicon. In Piland et al. [64], they attempted to observe the transfer through the change of photoluminescence (PL) transient of tetracene excitons. The exciton lifetimes are measured in a tetracene on hydrogen (H) passivated silicon sample. The paper showed no significant triplet excitons lifetime change with or without spacing layer (LiF), providing no evidence of triplet exciton transfer. On the other hand, singlet exciton transfer was observed from tetracene to silicon.

In this chapter, we would demonstrate and design an experimental setup for measuring triplet exciton transfer from tetracene to silicon. With the setup, we can then study and optimize the silicon surface for triplet exciton transfer.

6.2 Device Fabrication

Making a silicon solar cell with tetracene is on possible route for studying triplet energy transfer from tetracene to silicon. A device, however, is a complicated platform due to the presence of metal contacts and anti-reflection layers. To focus purely on optimizing the tetracene silicon interface, we instead measure the carrier population in silicon through photoluminescence. The tetracene/silicon device structures are shown

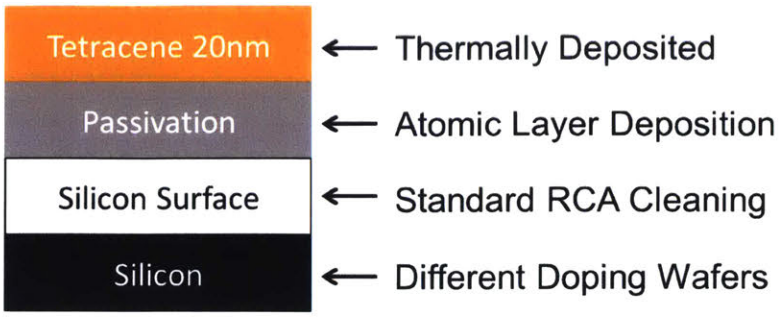

Figure 6-2: Structures and Fabrication of Tetracene/Silicon Devices. The silicon substrate are cleaned with standard RCA cleaning [11]. We can passivate the surface with H-termination with an HF etch (1% HF). The interface is then built from different material using atomic layer deposition (ALD). Finally, tetracene is deposited on the sample through thermal evaporation in vacuum chamber (2×10^{-6} torr).

in figure 6-2. The silicon substrates are cleaned with standard RCA cleaning [11]. First, it cleans the organic contaminants in 5:1:1 of deionized (DI) water, NH_4OH (29% by weight of NH_3), and hydrogen peroxide (30% H_2O_2) for 15 minutes, which the solution is heated to $75 - 85°C$. Then, the second step strips the native oxide in a room temperature 1% hydrofluoric acid for 30 seconds. The last step removes the metallic (ionic) contaminants in 6:1:1 of DI water, HCl (37% by weight), and 30% H_2O_2 for 10 minutes with solution temperature $75 - 85°C$. We then passivate the surface with H-termination with an HF etch (1% HF). The interface is then built from different materials using atomic layer deposition (ALD). Finally, tetracene is deposited on the sample through thermal evaporation in vacuum chamber (2×10^{-6} torr).

6.3 Magnetic Field Effect of Silicon Photoluminescence

From figure 3-9 in chapter 3, the magnetic field effect (MFE) is an ideal way to identify whether the measured signal is from singlet or triplet excitons. Therefore in this section, we examine triplet exciton transfer by measuring the MFE of silicon PL in a tetracene/silicon device based on figure 6-2.

6.3.1 Overlapping Emission Spectrum

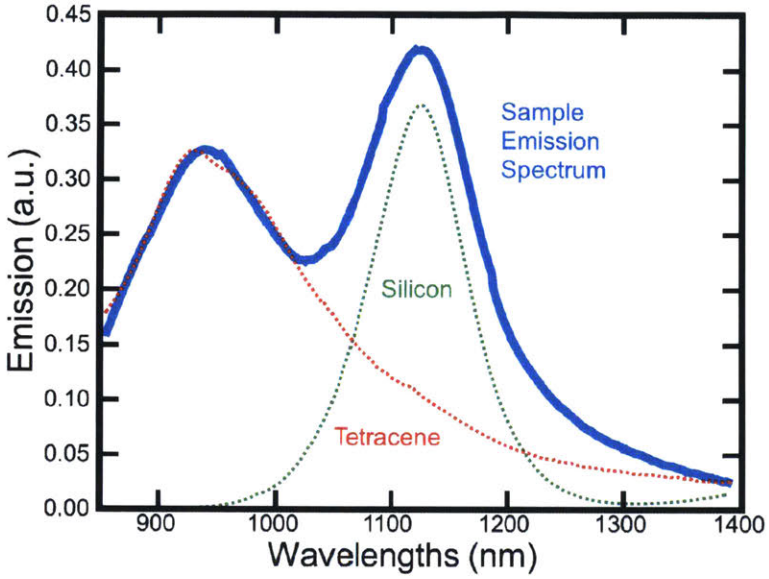

Figure 6-3: Emission Spectrum of a Tetracene/Silicon Device. The emission peak around 1100nm is from silicon, which matches to the silicon only PL spectrum in dashed green curve. The tetracene emission overlaps with silicon, shown in dashed red curve. The spectrometer response decreases for wavelengths below 950nm.

Silicon PL emits in the infrared around $\lambda = 1100$nm. However, silicon PL is extremely weak due to indirect band gap. In fact, the emission from silicon is so weak that extreme long wavelength tail of tetracene emission (assumed from singlet emission) in the infrared is comparable to silicon emission. A typical infrared spectrum measured in our tetracene/silicon device is shown in figure 6-3. The emission peak around 1100nm is from silicon, which matches the silicon-only PL spectrum in dotted green. On the left centered around $\lambda = 900$nm is the tetracene emission which overlaps with silicon emission.

Tetracene PL emission has a magnetic field effect, which was measured in figure 4-4. This will affect the MFE of silicon PL if we measure the PL by an infrared photodetector. Thus, we will need to measure the spectrally resolved MFE in order to separate the MFE of silicon and tetracene.

6.3.2 Measurement Setup

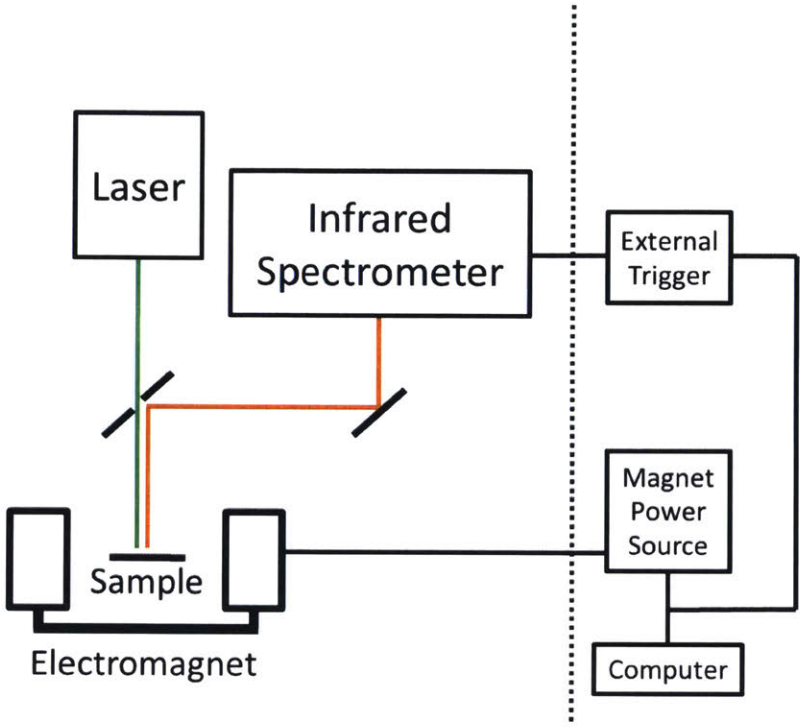

Figure 6-4: Spectrally Resolved Magnetic Field Effect Measurement Setup. This is the setup to measure the MFE of the silicon emission spectrum. The infrared spectrometer is a nitrogen cooled InGaAs spectrometer from Princeton Instrument. An external trigger (using a Keithley 2400) is used to control the spectrometer to acquire the spectrum through program.

To measure MFE of a spectrum, we modify the MFE setup shown in figure 4-2. In figure 6-4, a nitrogen cooled InGaAs spectrometer from Princeton Instruments is used to measure the infrared emission from silicon samples. The samples are placed in an electromagnet that can be controlled through a power source. The infrared spectrometer cannot be controlled through software due to the lack of API documentation. Thus, an external trigger (Keithley 2400) for the spectrometer is used for acquiring the spectrum.

Similar to the magnetic field effect measurement in figures 4-2 and 4-3, the change under a magnetic field is measured by applying on and off magnetic fields (B). Here, we measure the device emission spectrum and calculate the spectrum change/difference between on and off B.

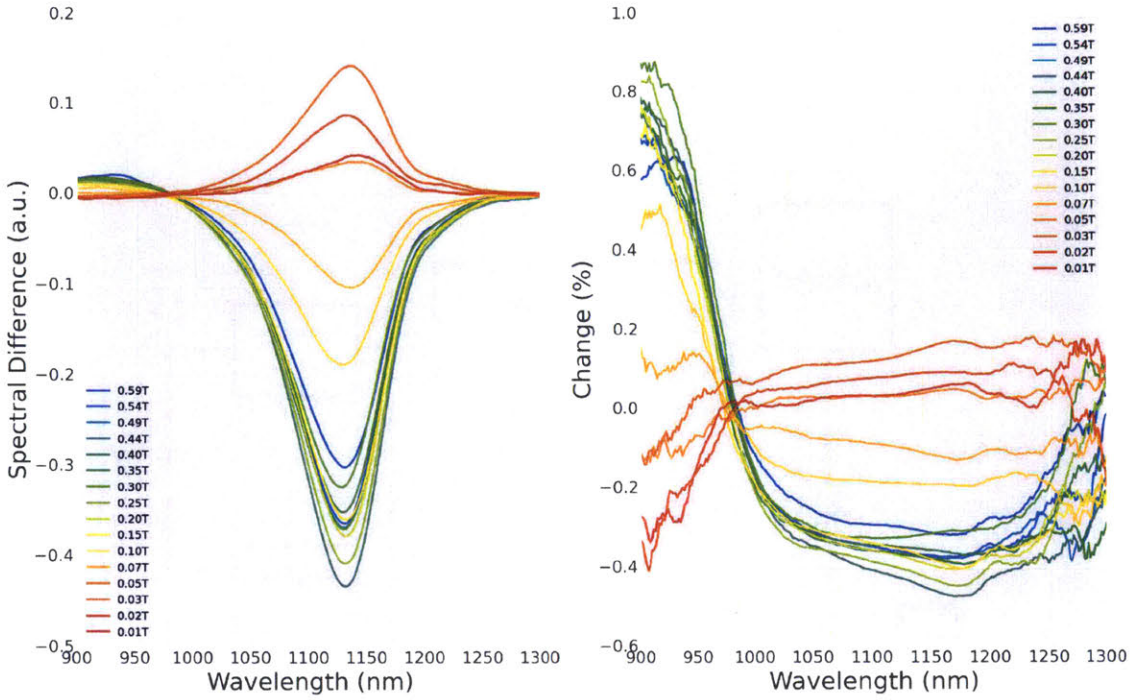

(a) Spectral Difference

(b) Spectral MFE

Figure 6-5: Spectrally Resolved MFE of a WN_x Passivated Sample. (a) The spectral difference of silicon PL between the on and off magnetic field. The silicon peak difference ($\sim$ 1100nm) is negative a large magnetic fields ($B > 0.05T$). The tetracene emission difference ($\sim$ 950nm) shows an increase with large magnetic field. (b) MFE change plotted as percentage change relative to emission intensity.

6.3.3 Spectrally Resolved Magnetic Field Effect on WN_x Passivated Sample

With the setup, we measured the MFE of the silicon spectrum with different passivation materials. Triplet exciton transfer from tetracene is observed with WN_x as the passivation layer on silicon. The WN_x passivated device structure (based on figure 6-2) consist of $\sim$10Å of SiO_x from RCA cleaning, 5 cycles of ALD of WN_x (expected to be $\sim$5Å but we have not confirmed its thickness) and 20nm of tetracene.

The differences of the silicon PL spectrum between magnetic field in its on and off states is plotted in figure 6-5a. From the result, we can see that the silicon peak is negative at ($\sim$ 1100nm) decreases with large magnetic fields ($B > 0.05T$). The tetracene emission difference ($\sim$ 950nm) shows an increase with large magnetic field.

In figure 6-5b, the MFE change could also be plotted in percentage change relative to emission intensity. As we can see, there is a clearly different regime above and below $\lambda = 975$nm, going from positive MFE to negative.

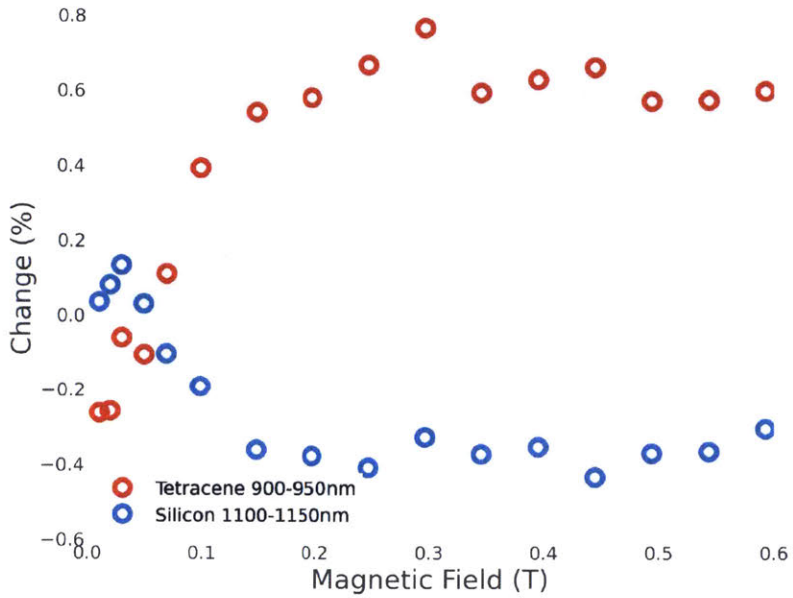

Figure 6-6: MFE for Different Spectral Range. The MFE of the silicon PL peak (1100-1150nm) is plotted in blue, showing a MFE trend similar to the triplet population MFE. This indicates that triplet excitons transfer and inject into silicon for a WN_x passivated sample. The MFE of the spectrum for tetracene emission (900-950nm) is plotted in red and has a similar trend to the singlet population MFE.

We can also plot the MFE of the emission integrated across different wavelength ranges. In figure 6-6, the MFE of the silicon PL peak (1100-1150nm) is plotted in blue. The silicon PL MFE has a trend similar to the triplet population MFE; see figure 3-9. This indicates that triplet excitons transfer and inject into silicon for a WN_x passivated sample. We also checked the MFE of the spectrum for wavelengths from 900 to 950nm (tetracene emission). The MFE of tetracene emission follows the trend of the singlet population MFE, which matches with the tetracene fluorescence MFE measured in figure 4-4.

From the spectrally resolved MFE, we have observed triplet exciton transfer from tetracene to silicon, specifically with WN_x as the passivation material for silicon surface. We have also confirmed in our experiment, that the silicon emission MFE

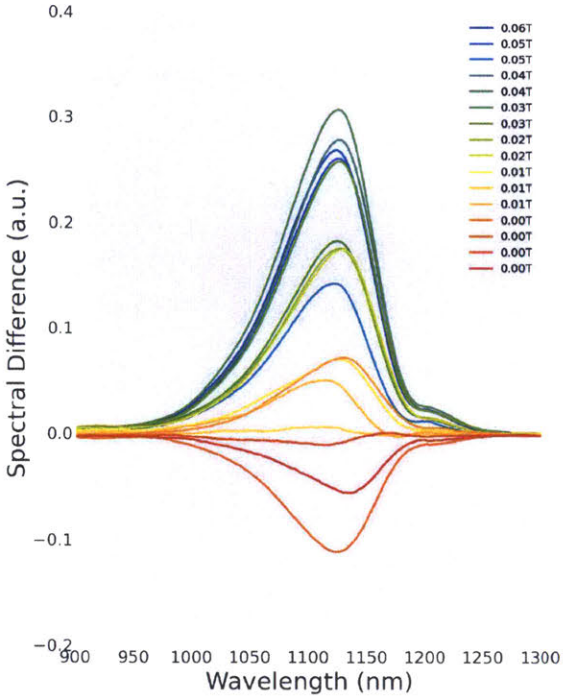

(a) Spectral Difference

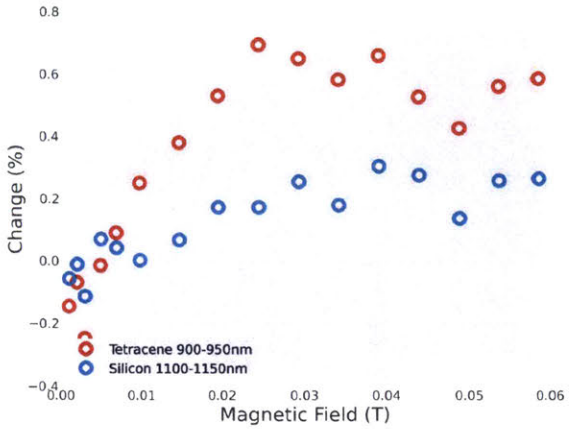

(b) Magnetic Field Effect

Figure 6-7: MFE of H-passivated/Tetracene Sample. (a) The spectral difference between and and off states of the magnetic field. Both the silicon PL and tetracene emission differences showed a positive MFE. (b) The MFE of tetracene emission (red) and peak MFE fo silicon PL (blue) are shown. Both MFE have similar trends to the singlet exciton population. This indicates at best inefficient triplet exciton transfer from tetracene to silicon.

remained similar to the triplet trend even though the tetracene emission MFE in IR showed singlet trend.

6.3.4 Passivations without Triplet Transfer

Here we repeated the spectrally resolved MFE on a H-terminated silicon sample with tetracene. The silicon samples are prepared with standard RCA cleaning, followed with an HF etch. The spectrally resolved MFE for the sample are measured; see figure 6-7. The spectral difference for magnetic field on and off are plotted in figure 6-7a. Both the silicon PL and tetracene emission differences showed positive MFE. The MFE of tetracene emission and the MFE at PL peak of silicon are calculated in figure 6-7b. Both MFE have similar trends to the singlet exciton population MFE.

This indicates at best inefficient triplet exciton transfer from tetracene to silicon. The results are consistent to the findings of Piland et al. [64] where no conclusive triplet exciton transfer was shown rather singlet exciton transfer was observed.

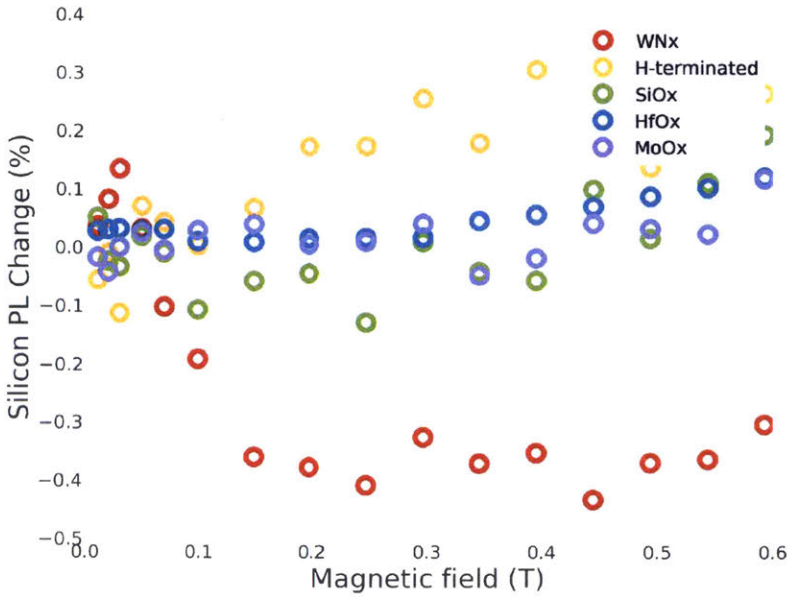

Figure 6-8: MFE of Silicon PL Peak with Different Passivation. The MFE of silicon PL are measured with WN_x and H-terminated passivation. Along with these, SiO_x, HfO_x, MoO_x passivation are also measured. Among these materials, only WN_x showed triplet MFE, indicating triplet exciton transfer.

We have also measured the MFE of silicon PL for various passivation materials. In figure 6-8, the MFE of three additional passivation materials SiO_x, HfO_x, MoO_x are measured. Along with H-passivated surfaces, these passivation materials showed no or slight MFE that are similar to the singlet MFE trend.

6.4 Excitation Spectrum of Silicon Photoluminescence

With the spectrally resolved MFE measurement, we have demonstrated triplet exciton transfer. In this section, we investigate the injected exciton yield by measuring excitation spectrum, that measures the PL intensity relative to excitation wavelengths. An example of using the excitation spectrum to determine the exciton transfer yield is demonstrated in figure 2 of Thompson et al. [65]. It is used to determine the total

exciton yield in tetracene and exciton transfer to quantum dots. Here we will discuss the excitation measurements and estimated exciton transfer yield for our WN_x passivated device.

6.4.1 Difficulties

There are some difficulties that needed to be overcome in order to measure the excitation spectrum in a tetracene/silicon device. Here we will address and provide solutions to the issues.

Overlapping PL Spectrum

In figure 6-3, the emission spectrum of the device consists of both tetracene and silicon emission. This makes it difficult to determine the silicon emission intensity using only photodetectors. To obtain the silicon emission intensity, we measure the spectrum and decompose the silicon peak emission and tetracene emission based on the individual spectra measured on plain silicon and tetracene on quartz.

Nonlinear Silicon PL and Laser Intensity Fluctuation

The silicon PLQY is not linear with excitation intensity. This is an important problem since the variable wavelength laser used (SuperK from NKT Photonics) has a large intensity variance across different wavelengths; see figure 6-9. Peak to peak intensity differences are up to a factor of 10. Measuring the excitation spectrum under such changes will yield data severely distorted by the laser wavelength response. To solve this issue, the laser intensity stabilized at a constant photon flux or intensity.

Silicon PLQY Dependency on Excitation Wavelength

The silicon PLQY by itself also changes with different excitation wavelengths. The main reason for wavelength dependence in silicon PL is the absorption depth. In silicon, high energy photons have higher absorption coefficients, thus are absorbed close to the surface, while the low energy photons are absorbed mainly in the bulk.

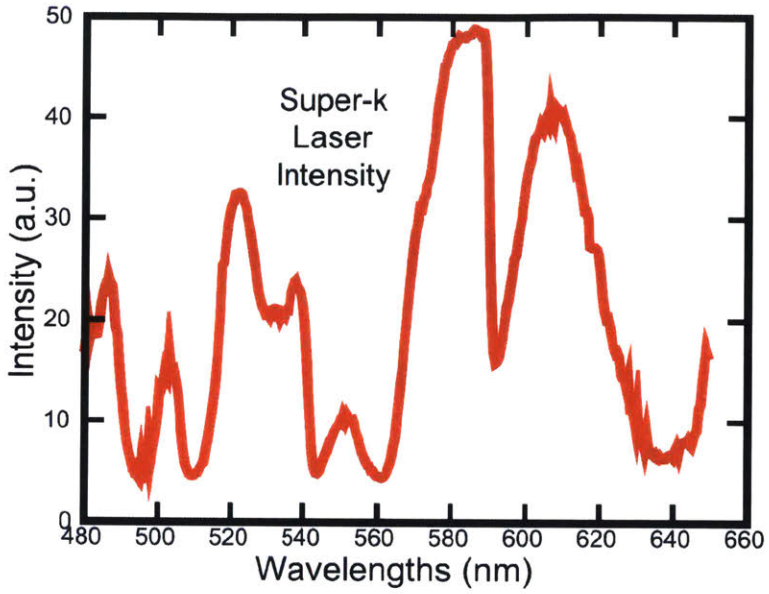

Figure 6-9: Variable Laser Source Intensity Changes. The Peak to peak intensity differences in our variable laser source (SuperK from NKT Photonics) are up to a factor of 10.

In semiconductors, the surface has many trap states with a higher quenching rate for the carriers. Therefore, short wavelength excitations in general have a lower PLQY, which is consistent with our measurements in figure 6-10. Due the PLQY wavelength dependencies, we need to measure the relative excitation spectrum by comparing the PL of silicon between samples with and without tetracene.

Systematic Error

Due to weak silicon PL, the experiment requires long excitation measurements, around 10 to 20 hours. This can introduce systematic errors such as material degradation in silicon or tetracene. If the PL of samples with or without tetracene excited at a given wavelength λ is measured separately for a few hours, the relative PL is hard to measure accurately. Therefore, the PL of samples with or without tetracene are measured in rapid succession.

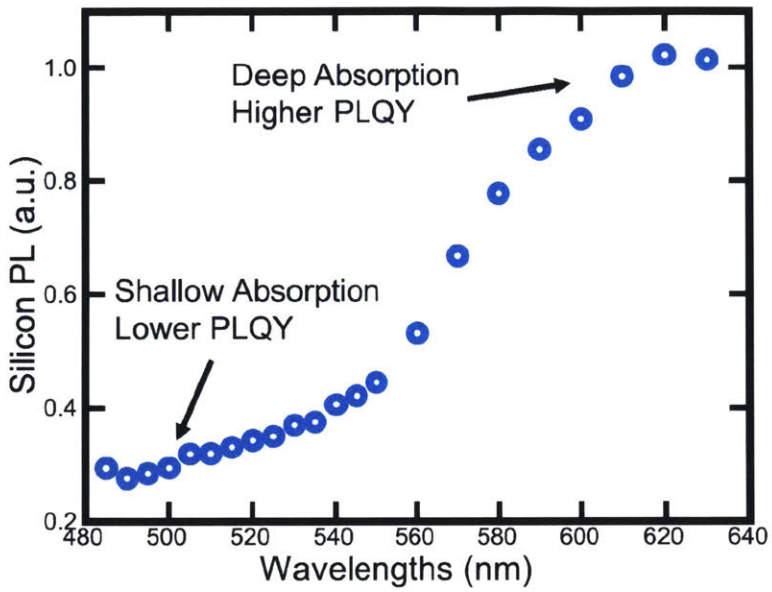

Figure 6-10: Measure Silicon PLQY with Different Excitation Wavelengths. The silicon PLQY decreases with shorter excitation wavelengths.

6.4.2 Measurement Setup

Based on the excitation spectrum measurement difficulties listed above, the improved excitation spectrum measurement setup is shown in diagram 6-11. The following details how the setup measures the excitation spectrum more accurately.

1. Overlapping PL spectrum. Using spectrometer instead of photodetector allows us to decompose the contributions of silicon and tetracene to the full emission spectrum.

2. Nonlinear silicon PL and laser intensity fluctuation. To avoid measuring an excitation spectrum distorted by laser intensity fluctuation, a beam splitter and a photodetector is used to measure the laser intensity. The laser source intensity can be changed, but the response of silicon PL is not linear. Therefore, we use the intensity feedback from the photodetector to stabilize the laser intensity. In our excitation spectrum, we stabilize the laser intensity such that the photon flux is constant.

3. Silicon PLQY dependency on excitation wavelength. To solve the issue, we com-

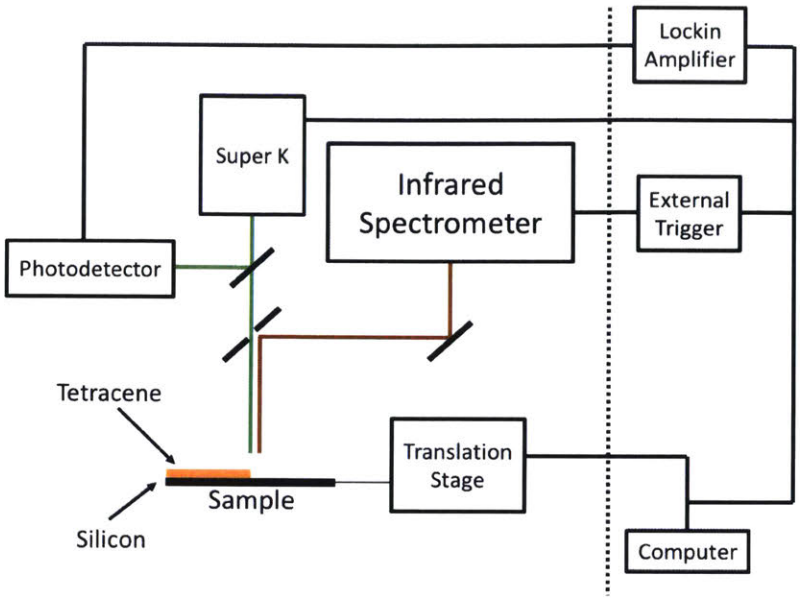

Figure 6-11: Excitation Spectrum Measurement Setup. To be able to measure the silicon PL, the infrared spectrometer is used to measure the emission spectrum. The variable laser source is a SuperK from NKT Photonics which allows different excitation wavelengths. The laser intensity is then measured and stabilized through a photodetector with a lock-in amplifier. The samples are held on a optical translation stage from Thorlabs that allows us to measure at different locations on the sample.

pare the relative excitation intensity between samples with or without tetracene.

4. Systematic error. Long measurements introduce systematic errors. To reduce the errors, the samples are prepared with half of the area deposited with tetracene. We employ a translation stage to switch between spots with and without tetracene and measure their silicon emission. Furthermore, the stage also moves the sample to a new location repeatedly to minimize degradation errors.

6.4.3 Excitation Spectrum of WN_x Passivated Sample

With the excitation measurement setup, we measured the excitation spectrum on the same WN_x passivated devices. The devices are made such that half of each sample is coated with 20nm thick tetracene. In figure 6-12, the silicon emission intensities for both are measured. For each excitation wavelength, multiple silicon PL

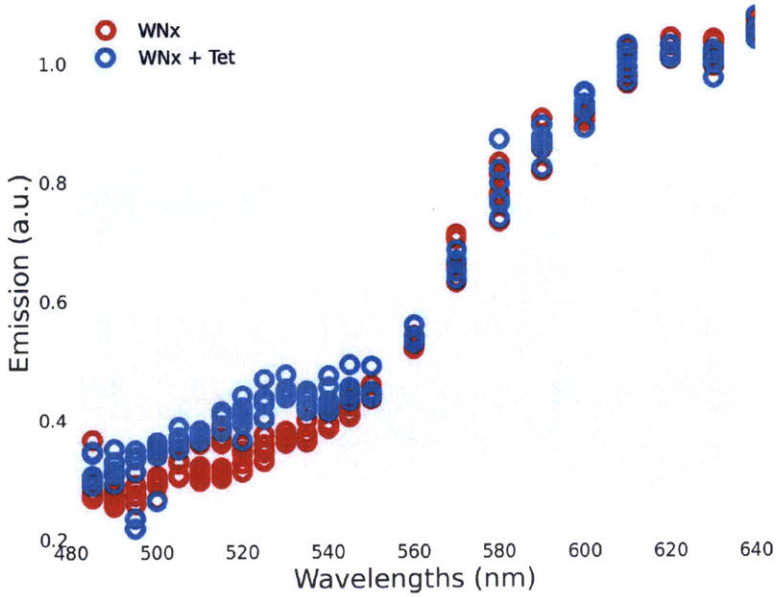

Figure 6-12: Silicon Emission of WN_x Passivated Samples. The blue circles are the silicon emission intensities of a sample with 20nm tetracene. The red circles are the emission of a plain sample. The sample has a same device structure in section 6.3.3. Multiple measurements are done for each excitation wavelengths.

are measurements acquired in different scans at different times and locations. With multiple location measurements, this reduces the optical geometric factor differences on the sample including tiny dust or non-uniformities in the packaging glass.

In figure 6-13, the relative excitation signal is calculated by averaging the emission at each wavelength in figure 6-12 and dividing the PL with tetracene by the PL without. The relative PL is then normalized with the values for wavelengths $\lambda >$ 600nm. The relative excitation values indicate the average increase in the silicon PL in tetracene samples as compared to normal samples. Therefore, the relative emission should be 1 for excitation wavelengths $>$ 550nm since tetracene does not absorb in the region. This is consistent with the measured excitation spectrum. For tetracene absorption wavelengths $<$ 540nm, there is an increase in the relative excitation spectrum that matches well with tetracene absorption spectrum, indicating that excitons in tetracene are injecting in the silicon.

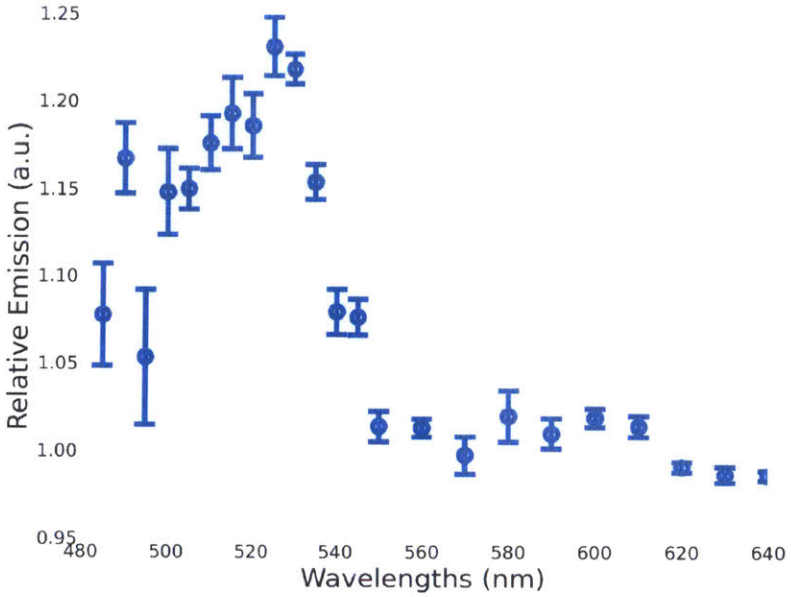

Figure 6-13: Excitation Spectrum of WN_x Passivated Samples. The relative excitation signal is calculated by averaging the emission at each wavelength in figure 6-12 and dividing the PL with tetracene to the PL without. The relative PL is then normalized with the values from > 600nm. An increase in the excitation spectrum is measured at the wavelengths where tetracene absorbs $\lambda < 540$nm. The error bars are also calculated and are larger in the tetracene absorption range due to errors introduced during spectrum decomposition.

6.4.4 Model of Excitation Spectrum

To calculate the yield of the total exciton injection from tetracene to silicon, we need to create a model for the relative excitation spectrum. The total silicon PL from sample with and without tetracene is,

$$PL_w(\lambda) = A_{w,Si}(\lambda)\eta_{si}(\lambda) + A_{w,tet}(\lambda)\eta_{fis}\eta_{tran}\eta_{inj} \tag{6.1}$$

$$PL_o(\lambda) = A_{o,Si}(\lambda)\eta_{si}(\lambda) \tag{6.2}$$

where the subscripts w, o indicates the values with and without tetracene, respectively. A is the respective material absorption which depends on wavelengths and can be calculated with the transfer matrix method. ηs are the efficiencies including the fission efficiency in tetracene η_{fis} and the exciton transfer efficiency from tetracene to silicon. Usually, in molecular materials the PL efficiencies are constant. However,

in our device, the silicon PL efficiency depends on the excitation wavelength. But we assume the injected carriers have a constant PL efficiency. The relative excitation spectrum is then expressed as,

$$E(\lambda) = \frac{PL_w(\lambda)}{PL_o(\lambda)} = \frac{A_{w,Si}(\lambda) + A_{w,tet}(\lambda)\eta_{fis}\eta_{tran}\eta_{inj}/\eta_{si}(\lambda)}{A_{o,Si}(\lambda)} \tag{6.3}$$

The absorption is calculated from transfer matrix and the silicon PLQY for our device is measured. Unfortunately, it is hard to separate the injected carrier PL efficiency η_{inj} with the $\eta_{fis}\eta_{tran}$, which is the total efficiency we would like to obtain. Therefore, in this work, η_{inj} is conservatively assumed to be the maximum silicon PL efficiency we measured in the experiment, which is $\eta_{inj} = \eta_{si}(\lambda = 640\text{nm})$. From the silicon PLQY in figure 6-10, we can see that the silicon PLQY is slowly saturating towards infrared. The calculated $\eta_{eff} = \eta_{fis}\eta_{tran}$ is our estimated lower bound for down conversion efficiency from tetracene.

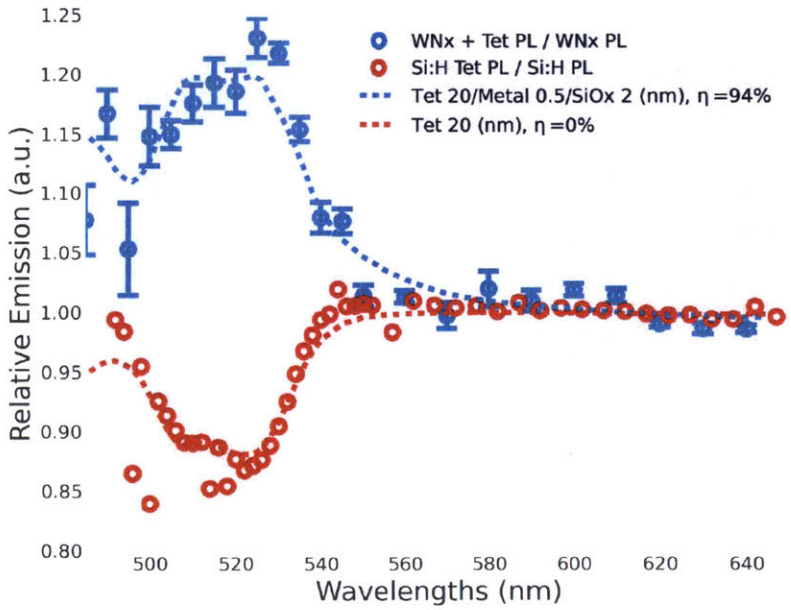

Figure 6-14: Excitation Spectrum with Modeling. The blue circles are the excitation spectrum from a WN_x passivated sample, where the red circles are measured from the H-passivated sample. The dashed lines are the fitted model for respective excitation spectra.

In figure 6-14, the excitation spectrum of WN_x passivated sample fits fairly well with $\eta_{eff} = 94\%$. The efficiency didn't exceed 100% but this is a fairly conservative estimation of the down conversion efficiency from tetracene. The n, k for WN_x are estimated with aluminum due to the metallic nature of WN_x. However, the differences are small due to thin WN_x layer. In the figure, the excitation spectrum for H-passivated device are also measured. The relative emission in tetracene absorption range decreases. The excitation spectrum of H-passivated samples fit very well with our model where $\eta_{eff} = 0\%$. This once again is consistent with our result that there is negligible triplet exciton transfer from tetracene to an H-passivated sample.

6.5 Further Investigations of Triplet Transfer

With the results in this chapter, we have demonstrated triplet exciton transfer from tetracene to silicon and also estimated a lower bound for the efficiency of exciton transfer. However, the mechanisms for the effects at WN_x interfaces remain uncertain. Consequently, we have performed some additional characterization.

6.5.1 Thickness Dependence of WN_x

The first check is how the thickness of WN_x affects triplet exciton transfer from tetracene to silicon. The MFE for $B > 0.4T$ with different WN_x passivation thicknesses are measured, plotted in figure 6-15. For thin layers of WN_x passivations, the silicon PL has smaller MFE changes. This is expected since the silicon PL for no passivation of WN_x did not show a triplet MFE trend (figure 6-8). However, for thick WN_x layers, the MFE decreases to zero which indicates that thick passivation layers block exciton transfer. This result indicates WN_x passivation mediates the triplet exciton for short range transfer.

It is important to note that the thickness of WN_x has not been fully characterized. From preliminary data, the growth of WN_x does not appear to be linear with the number of ALD cycles. Nevertheless, the MFE dependencies on thickness is consistent with observations that WN_x mediates triplet exciton transfer.

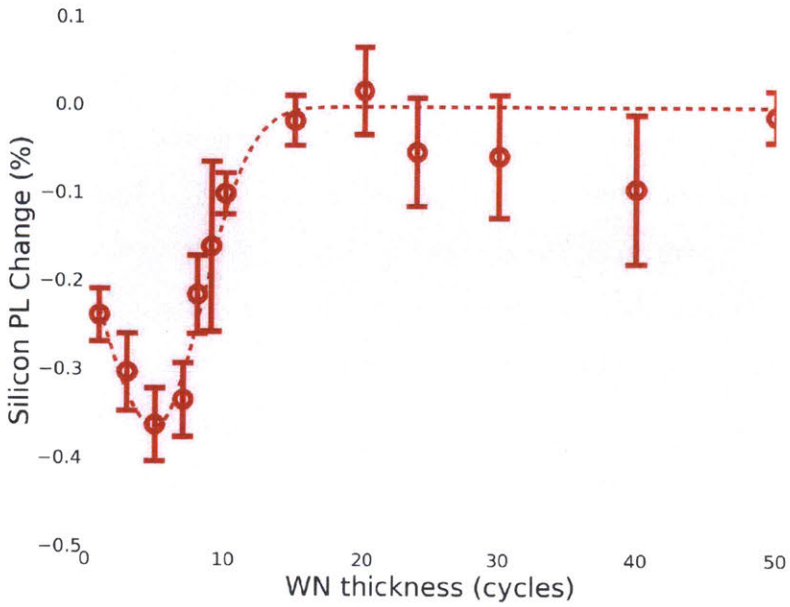

Figure 6-15: MFE Dependencies on WN_x Passivation Thicknesses. The MFE for $B > 0.4T$ with different WN_x passivation thickness are measured. The MFE increases with several cycles for WN_x and decreases at thick layers.

6.5.2 Doping Level

One interesting aspect to know is how the triplet exciton transfer with different doping levels in silicon wafer. This study may help us know whether if the energy alignments at the interface affect electron or hole injection. In figure 6-16, the large magnetic field ($B > 0.4T$) MFE is measured for silicon wafers with different doping levels of silicon wafers. The doping level are expressed in calculated Fermi energy differences ΔE_F from the intrinsic silicon Fermi energy. There are no clear differences or trends from $\Delta E_F = -0.4$eV to 0.4eV. However, for the heavily doped wafers, the transfer does not work as well compared to the lightly doped silicon wafers.

This result demonstrates that energy alignment between the bulk silicon and tetracene might not matter that much. One reason could be that WN_x passivation may be more important to the energy alignment or some other mechanism for exciton transfer. This experiment also helps us eliminate the possibility of a "charging effect" enhancement. "Charging effect" is a hypothesis that the excitons are dissociated in tetracene and WN_x. The charged tetracene may form a gate bias on the

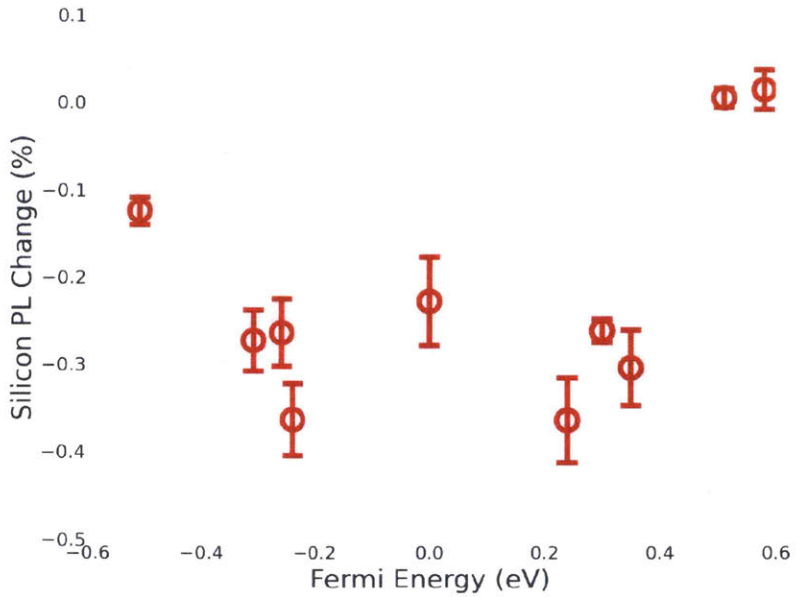

Figure 6-16: MFE of Silicon PL with Different Doping Levels. The large magnetic field ($B > 0.4T$) MFE are measured with different doping levels of silicon wafers. All of the device have WN_x passiavation with 20nm of tetracene deposited on top.

silicon surface and affect the PLQY of the silicon. For example, if a p-type wafer is biased with a positive voltage that attracts some electrons to the surface, this may reduce majority carriers and increase silicon PL efficiencies. However, this experiment showed PL influence from triplet excitons with p, n-type and intrinsic wafers, which disproves the charging effect.

6.5.3 Red-Green MFE Experiment

Another investigation of the triplet transfer mechanism is the red-green simultaneous excitation MFE experiment. When exciting the tetracene, the photons are not fully absorbed by the tetracene and still excite the silicon. This creates some carriers in silicon. If these carriers' PL efficiencies are enhanced by the triplets directly or indirectly, the silicon PL may have MFE that is similar to the triplet exciton MFE while not originating in triplet energy transfer. A potential mechanism could be the charging effect in tetracene that was mentioned above, or trap state filling at the surface. If these mechanisms are the reason for the MFE measured, then the

tetracene cannot enhance the solar cell efficiency by injecting more carriers for high energy photons.

This experiment is designed with the idea that excitons created in tetracene may influence the carrier PL efficiency in silicon. Red excitations $\lambda > 550$nm are only absorbed in silicon hence they should not have MFE. Measuring the red excitation PL under green excitation bias would indicate whether excitons in tetracene are injecting into silicon and affecting the carriers remotely. If excitons are injecting carriers into silicon, the excitons in tetracene should not affect the red excitation PL. For remote effect, the excitons should influence red excited carriers. The experiment is designed with a constant green excitation $\lambda = 532$nm while measuring the PL with and without red excitation. The difference would then be the red excitation PL signal. We then measure the MFE of this red excitation PL.

However, the injected carriers can influence the carriers' PL efficiency due to the non-linear silicon PLQY. Here is a simple demonstration of how injected excitons from green absorption may influence red excitation PL.

$$\begin{aligned} PL_g &= kn_g^2 \\ \delta PL_g &= \frac{n_g(H)^2 - n_g(0)^2}{n_g(0)^2} \approx 2\delta n_g \end{aligned} \tag{6.4}$$

$$\begin{aligned} PL_r &= k(n_g + n_r)^2 - kn_g^2 = k(2n_g n_r + n_r^2) \\ \delta PL_r &= \frac{2n_r(n_g(H) - n_g(0))}{2n_g(0)n_r + n_r^2} = \delta n_g \left(\frac{1}{1 + \frac{n_r}{2n_g(0)}} \right) \end{aligned} \tag{6.5}$$

The red excitation MFE δPL_r could be up to $0.5\delta PL_g$ when the density of absorbed green excitation carriers is much larger than the red excitation carriers $n_g \gg n_r$. In fact, our first experiment where green excitation are much larger then red excitation showed green MFE $= -0.713\%$ and red excitation MFE $= -0.356\%$. In our second red-green experiment, the red excitation intensity was much larger. This showed -0.048% for the red excitation PL MFE indicating exciton injection from tetracene to silicon. However, the green MFE in this measurement is 0.516%, differ-

ent to the expected negative MFE. The green excitation used in this measurement is much lower than the red excitation intensity. The estimated decomposition error for silicon PL intensity if 57.2 times more for green excitation than red excitation.

6.6 Conclusion on Triplet Exciton Transfer

In this work, we have shown triplet exciton transfer from tetracene to silicon, proven by designing a spectrally resolved MFE experiment. It is also worth noting that among the passivation we have tried, WN_x is the one we have found successfully triplet transfer from tetracene to silicon.

The excitation spectrum are also measured on a WN_x passivated sample. We have designed an excitation spectrum measurement setup that allows us to measure from the weak silicon PL. The fission plus transfer efficiency is estimated with a lower bound of 92%.

The mechanism of how exciton transfer from tetracene to silicon is currently unknown despite some efforts on trying to understand the surface passivation. However, we believe this a big step towards realizing down conversion in silicon solar cell.

Chapter 7

Conclusion and Future Work

7.1 Conclusion

In this thesis, we have shown improvement in both energy down conversion and up conversion.

We demonstrate an optical up conversion device utilizing triplet-triplet annihilation and TADF molecules. TADF materials as triplet exciton sensitizers are promising because their small singlet-triplet splitting brings closer to the ideal case of halving the wavelength during up conversion, and the absence of heavy metals could lower the cost if this technology becomes widespread. Thus, our design opens the door to the inexpensive sensitizer materials that show up conversion in solid state structures.

For down conversion, the ultimate goal is to pair an efficient down conversion material with a low energy material, to improve the solar cell power conversion efficiencies. We investigated tetracene because the energy levels are suitable for the low energy material silicon. Silicon is one of the cheapest and most used solar cell material. Pursuing this material choice, we have determined efficient singlet fission efficiencies in tetracene with maximum IQE of 127% and triplet yields up to 192%. We then demonstrated triplet exciton from tetracene to silicon. The transfer was confirmed by designing a spectrally resolved MFE experiment. It is also worth noting that we have found WN_x to be a passivation material that allows triplet transfer from tetracene to silicon. The fission plus transfer efficiency is estimated with a lower

bound of 92% in a relative excitation spectrum measurement.

7.2 Future Road for the Project

There are potentially many projects to extend the work in this thesis. For optical up conversion, a full solid state fabrication opens the more possibility of new device structures, such as co-deposited layers and the stacking of multiple devices to improve the total absorption. The use of TADF materials also open up more choices for optical up conversion.

In the tetracene down converter project, there are still some milestones before fully realizing a tetracene silicon hybrid solar cell that overcomes Shockley-Queisser limit. One project is to understand what makes WN_x special, allowing triplet exciton transfer between organics that semiconductors. WN_x makes the silicon PL much darker, thus an alternative material that also allows transfer is needed. Another experiment is to demonstrate triplet transfer in a silicon solar cell device and measure the total efficiency from tetracene. Many device structures have been proposed, such as a simple metal-insulator-semiconductor solar cell that reduces the fabrication complexity without heavily doping the silicon wafer. However, this still requires metal contacts in between the tetracene and the silicon interface. The Sunpower solar cell [66] structure is another design that has its doped regions and contacts in the back. This provides a clean surface on top that allows us to engineer the passivation and deposit tetracene. Another milestone would be engineering the surface such that tetracene has maximum absorption while maintaining high IQE. This requires surface structure engineering or optical trapping for tetracene. These experiments are essential before pushing the efficiency in a tetracene silicon down conversion solar cell.

Appendix A

Publications

A.1 Singlet Fission and Triplet-Triplet Annihilation

1. Tony C Wu, Nicholas J Thompson, Daniel N Congreve, Eric Hontz, Shane R Yost, Troy Van Voorhis, and Marc A Baldo. Singlet fission efficiency in tetracene-based organic solar cells. *Applied Physics Letters*, 104(19):193901, 2014

2. Shane R Yost, Jiye Lee, Mark WB Wilson, Tony Wu, David P McMahon, Rebecca R Parkhurst, Nicholas J Thompson, Daniel N Congreve, Akshay Rao, Kerr Johnson, et al. A transferable model for singlet-fission kinetics. *Nature chemistry*, 6(6):492, 2014

3. Wendi Chang, Daniel N Congreve, Eric Hontz, Matthias E Bahlke, David P McMahon, Sebastian Reineke, Tony C Wu, Vladimir Bulovic, Troy Van Voorhis, and Marc A Baldo. Spin-dependent charge transfer state design rules in organic photovoltaics. *Nature communications*, 6:6415, 2015

4. Tony C Wu, Daniel N Congreve, and Marc A Baldo. Solid state photon upconversion utilizing thermally activated delayed fluorescence molecules as triplet sensitizer. *Applied Physics Letters*, 107(3):031103, 2015

A.2 Thermally Activated Delayed Fluorescence

1. Katsuaki Kawasumi, Tony Wu, Tianyu Zhu, Hyun Sik Chae, Troy Van Voorhis, Marc A Baldo, and Timothy M Swager. Thermally activated delayed fluorescence materials based on homoconjugation effect of donor–acceptor triptycenes. *Journal of the American Chemical Society*, 137(37):11908–11911, 2015

2. Gregory D Gutierrez, Graham T Sazama, Tony Wu, Marc A Baldo, and Timothy M Swager. Red phosphorescence from benzo [2, 1, 3] thiadiazoles at room temperature. *The Journal of organic chemistry*, 81(11):4789–4796, 2016

3. Aleksandr V Zhukhovitskiy, Michael G Mavros, KT Queeney, Tony Wu, Troy Van Voorhis, and Jeremiah A Johnson. Reactions of persistent carbenes with hydrogen-terminated silicon surfaces. *Journal of the American Chemical Society*, 138(27):8639–8652, 2016

4. Rafael Gómez-Bombarelli, Jorge Aguilera-Iparraguirre, Timothy D Hirzel, David Duvenaud, Dougal Maclaurin, Martin A Blood-Forsythe, Hyun Sik Chae, Markus Einzinger, Dong-Gwang Ha, Tony Wu, et al. Design of efficient molecular organic light-emitting diodes by a high-throughput virtual screening and experimental approach. *Nature Materials*, 15(10):1120–1127, 2016

Bibliography

[1] David L Dexter. A theory of sensitized luminescence in solids. *The Journal of Chemical Physics*, 21(5):836–850, 1953.

[2] Th Förster. Zwischenmolekulare energiewanderung und fluoreszenz. *Annalen der physik*, 437(1-2):55–75, 1948.

[3] William Shockley and Hans J Queisser. Detailed balance limit of efficiency of p-n junction solar cells. *Journal of applied physics*, 32(3):510–519, 1961.

[4] Solar spectra (nrel, http://rredc.nrel.gov/solar/spectra/).

[5] RC Johnson and RE Merrifield. Effects of magnetic fields on the mutual annihilation of triplet excitons in anthracene crystals. *Physical Review B*, 1(2):896, 1970.

[6] Daniel N Congreve, Jiye Lee, Nicholas J Thompson, Eric Hontz, Shane R Yost, Philip D Reusswig, Matthias E Bahlke, Sebastian Reineke, Troy Van Voorhis, and Marc a Baldo. External quantum efficiency above 100% in a singlet-exciton-fission-based organic photovoltaic cell. *Science*, 340(6130):334–7, 2013.

[7] Sungyeop Jung, Kyoung-Youm Kim, Yeon-Il Lee, Jun-Ho Youn, Hie-Tae Moon, Jin Jang, and Jungho Kim. Optical modeling and analysis of organic solar cells with coherent multilayers and incoherent glass substrate using generalized transfer matrix method. *Japanese Journal of Applied Physics*, 50(12R):122301, 2011.

[8] Shane R Yost, Jiye Lee, Mark WB Wilson, Tony Wu, David P McMahon, Rebecca R Parkhurst, Nicholas J Thompson, Daniel N Congreve, Akshay Rao, Kerr Johnson, et al. A transferable model for singlet-fission kinetics. *Nature chemistry*, 6(6):492, 2014.

[9] Cheng-Lung Wu, Che-Hong Chang, Yung-Ting Chang, Chin-Ti Chen, Chao-Tsen Chen, and Chi-Jung Su. High efficiency non-dopant blue organic light-emitting diodes based on anthracene-based fluorophores with molecular design of charge transport and red-shifted emission proof. *Journal of Materials Chemistry C*, 2(35):7188–7200, 2014.

[10] Atula SD Sandanayaka, Kou Yoshida, Toshinori Matsushima, and Chihaya Adachi. Exciton quenching behavior of thermally activated delayed fluorescence molecules by charge carriers. *The Journal of Physical Chemistry C*, 119(14):7631–7636, 2015.

[11] Werner Kern. The evolution of silicon wafer cleaning technology. *Journal of the Electrochemical Society*, 137(6):1887–1892, 1990.

[12] RC Johnson, RE Merrifield, P Avakian, and RB Flippen. Effects of magnetic fields on the mutual annihilation of triplet excitons in molecular crystals. *Physical Review Letters*, 19(6):285, 1967.

[13] RE Merrifield, P Avakian, and RP Groff. Fission of singlet excitons into pairs of triplet excitons in tetracene crystals. *Chemical Physics Letters*, 3(6):386–388, 1969.

[14] Millicent B Smith and Josef Michl. Singlet fission. *Chemical reviews*, 110(11):6891–6936, 2010.

[15] Ramamurti Shankar. *Principles of quantum mechanics*. Springer Science & Business Media, 2012.

[16] M Pope and C. E. Napolitano. *Electronic processes in organic crystals andpolymers*. Oxford University Press, 1999.

[17] Martin Pope and Charles E Swenberg. *Electronic processes in organic crystals and polymers*. Oxford University Press on Demand, 1999.

[18] Jingbo Zhao, Yunke Li, Guofang Yang, Kui Jiang, Haoran Lin, Harald Ade, Wei Ma, and He Yan. Efficient organic solar cells processed from hydrocarbon solvents. *Nature Energy*, 1:15027, 2016.

[19] Kunta Yoshikawa, Hayato Kawasaki, Wataru Yoshida, Toru Irie, Katsunori Konishi, Kunihiro Nakano, Toshihiko Uto, Daisuke Adachi, Masanori Kanematsu, Hisashi Uzu, et al. Silicon heterojunction solar cell with interdigitated back contacts for a photoconversion efficiency over 26%. *Nature Energy*, 2:17032, 2017.

[20] T Trupke, MA Green, and P Würfel. Improving solar cell efficiencies by down-conversion of high-energy photons. *Journal of applied physics*, 92(3):1668–1674, 2002.

[21] Martin A Green and Stephen P Bremner. Energy conversion approaches and materials for high-efficiency photovoltaics. *Nature materials*, 16(1):23–34, 2017.

[22] T Trupke, MA Green, and P Würfel. Improving solar cell efficiencies by up-conversion of sub-band-gap light. *Journal of Applied Physics*, 92(7):4117–4122, 2002.

[23] Thorsten Trupke, Avi Shalav, BS Richards, P Würfel, and MA Green. Efficiency enhancement of solar cells by luminescent up-conversion of sunlight. *Solar Energy Materials and Solar Cells*, 90(18):3327–3338, 2006.

[24] BS Richards. Luminescent layers for enhanced silicon solar cell performance: Down-conversion. *Solar energy materials and solar cells*, 90(9):1189–1207, 2006.

[25] Jiazhong Zhang, Haiping Xia, Yongzhang Jiang, Shuo Yang, Haochuan Jiang, and Baojiu Chen. Efficient quantum cutting in tb 3+/yb 3+ codoped α-nayf 4 single crystals grown by bridgman method using kf flux for solar photovoltaic. *IEEE Journal of Quantum Electronics*, 51(6):1–6, 2015.

[26] M Chabr, UP Wild, J Fünfschilling, and I Zschokke-Gränacher. Quantum beats of prompt fluorescence in tetracene crystals. *Chemical Physics*, 57(3):425–430, 1981.

[27] Jonathan J Burdett and Christopher J Bardeen. Quantum beats in crystalline tetracene delayed fluorescence due to triplet pair coherences produced by direct singlet fission. *Journal of the American Chemical Society*, 134(20):8597–8607, 2012.

[28] Nicholas J Thompson, Eric Hontz, Daniel N Congreve, Matthias E Bahlke, Sebastian Reineke, Troy Van Voorhis, and Marc A Baldo. Nanostructured singlet fission photovoltaics subject to triplet-charge annihilation. *Advanced Materials*, 26(9):1366–1371, 2014.

[29] S Singh, WJ Jones, W Siebrand, BP Stoicheff, and WG Schneider. Laser generation of excitons and fluorescence in anthracene crystals. *The Journal of Chemical Physics*, 42(1):330–342, 1965.

[30] RP Groff, P Avakian, and RE Merrifield. Coexistence of exciton fission and fusion in tetracene crystals. *Physical Review B*, 1(2):815, 1970.

[31] AJ Nozik, RJ Ellingson, OI Mićić, JL Blackburn, P Yu, JE Murphy, MC Beard, and G Rumbles. Unique approaches to solar photon conversion based on semiconductor nanostructures and novel molecular chromophores; dynamics of electron relaxation, interfacial charge transfer, and carrier multiplication. In *Proceedings of the 27th DOE Solar Photochemistry Research Conference*, pages 63–66. Airline Conference Center Warrenton, VA, 2004.

[32] Radiy R Islangulov, Denis V Kozlov, and Felix N Castellano. Low power upconversion using mlct sensitizers. *Chemical Communications*, (30):3776–3778, 2005.

[33] Chen Wang and Michael J Tauber. High-yield singlet fission in a zeaxanthin aggregate observed by picosecond resonance raman spectroscopy. *Journal of the American Chemical Society*, 132(40):13988–13991, 2010.

[34] M Tuan Trinh, Yu Zhong, Qishui Chen, Theanne Schiros, Steffen Jockusch, Matthew Y Sfeir, Michael Steigerwald, Colin Nuckolls, and Xiaoyang Zhu. Intra-to intermolecular singlet fission. *The Journal of Physical Chemistry C*, 119(3):1312–1319, 2015.

[35] Irina Paci, Justin C Johnson, Xudong Chen, Geeta Rana, Duška Popović, Donald E David, Arthur J Nozik, Mark A Ratner, and Josef Michl. Singlet fission for dye-sensitized solar cells: Can a suitable sensitizer be found? *Journal of the American Chemical Society*, 128(51):16546–16553, 2006.

[36] Priya J Jadhav, Aseema Mohanty, Jason Sussman, Jiye Lee, and Marc A Baldo. Singlet exciton fission in nanostructured organic solar cells. *Nano letters*, 11(4):1495–1498, 2011.

[37] Alex Hayat, Pavel Ginzburg, and Meir Orenstein. Observation of two-photon emission from semiconductors. *Nature photonics*, 2(4):238–241, 2008.

[38] Mengfei Wu, Daniel N Congreve, Mark WB Wilson, Joel Jean, Nadav Geva, Matthew Welborn, Troy Van Voorhis, Vladimir Bulović, Moungi G Bawendi, and Marc A Baldo. Solid-state infrared-to-visible upconversion sensitized by colloidal nanocrystals. *Nature Photonics*, 10(1):31–34, 2016.

[39] Y Tomkiewicz, RP Groff, and P Avakian. Spectroscopic approach to energetics of exciton fission and fusion in tetracene crystals. *The Journal of Chemical Physics*, 54(10):4504–4507, 1971.

[40] NE Geacintov, J Burgos, M Pope, and C Strom. Heterofission of pentacene excited singlets in pentacene-doped tetracene crystals. *Chemical Physics Letters*, 11(4):504–508, 1971.

[41] J Burgos, M Pope, Ch E Swenberg, and RR Alfano. Heterofission in pentacene-doped tetracene single crystals. *physica status solidi (b)*, 83(1):249–256, 1977.

[42] Wai-Lun Chan, Manuel Ligges, Askat Jailaubekov, Loren Kaake, Luis Miaja-Avila, and X-Y Zhu. Observing the multiexciton state in singlet fission and ensuing ultrafast multielectron transfer. *Science*, 334(6062):1541–1545, 2011.

[43] Verner K Thorsmølle, Richard D Averitt, Jure Demsar, DL Smith, S Tretiak, RL Martin, X Chi, BK Crone, AP Ramirez, and AJ Taylor. Morphology effectively controls singlet-triplet exciton relaxation and charge transport in organic semiconductors. *Physical Review Letters*, 102(1):017401, 2009.

[44] Jonathan J Burdett, Astrid M Müller, David Gosztola, and Christopher J Bardeen. Excited state dynamics in solid and monomeric tetracene: The roles of superradiance and exciton fission. *The Journal of chemical physics*, 133(14):144506, 2010.

[45] Tony C Wu, Nicholas J Thompson, Daniel N Congreve, Eric Hontz, Shane R Yost, Troy Van Voorhis, and Marc A Baldo. Singlet fission efficiency in tetracene-based organic solar cells. *Applied Physics Letters*, 104(19):193901, 2014.

[46] Phil D Reusswig, Daniel N Congreve, Nicholas J Thompson, and Marc A Baldo. Enhanced external quantum efficiency in an organic photovoltaic cell via singlet fission exciton sensitizer. *Applied Physics Letters*, 101(11):113304, 2012.

[47] Jiye Lee, Priya Jadhav, and MA Baldo. High efficiency organic multilayer photodetectors based on singlet exciton fission. *Applied physics letters*, 95(3):192, 2009.

[48] Mark WB Wilson, Akshay Rao, Kerr Johnson, Simon GeÌĄlinas, Riccardo Di Pietro, Jenny Clark, and Richard H Friend. Temperature-independent singlet exciton fission in tetracene. *Journal of the American Chemical Society*, 135(44):16680–16688, 2013.

[49] Hermann Anton Haus. *Waves and Fields in Optoelectronics*. Prentice Hall, 1983.

[50] George F Burkhard, Eric T Hoke, and Michael D McGehee. Accounting for interference, scattering, and electrode absorption to make accurate internal quantum efficiency measurements in organic and other thin solar cells. *Advanced Materials*, 22(30):3293–3297, 2010.

[51] Jonathan J Burdett, David Gosztola, and Christopher J Bardeen. The dependence of singlet exciton relaxation on excitation density and temperature in polycrystalline tetracene thin films: Kinetic evidence for a dark intermediate state and implications for singlet fission. *The Journal of chemical physics*, 135(21):214508, 2011.

[52] S Arnold, RR Alfano, M Pope, W Yu, P Ho, R Selsby, J Tharrats, and CE Swenberg. Triplet exciton caging in two dimensions. *The Journal of Chemical Physics*, 64(12):5104–5114, 1976.

[53] Philip C Boutin, Kenneth P Ghiggino, Timothy L Kelly, and Ronald P Steer. Photon upconversion by triplet–triplet annihilation in ru (bpy) 3-and dpa-functionalized polymers. *The Journal of Physical Chemistry Letters*, 4(23):4113–4118, 2013.

[54] Soo Hyon Lee, Mathieu A Ayer, Roberto Vadrucci, Christoph Weder, and Yoan C Simon. Light upconversion by triplet–triplet annihilation in diphenylanthracene-based copolymers. *Polymer Chemistry*, 5(24):6898–6904, 2014.

[55] Tony C Wu, Daniel N Congreve, and Marc A Baldo. Solid state photon upconversion utilizing thermally activated delayed fluorescence molecules as triplet sensitizer. *Applied Physics Letters*, 107(3):031103, 2015.

[56] Hiroki Uoyama, Kenichi Goushi, Katsuyuki Shizu, Hiroko Nomura, and Chihaya Adachi. Highly efficient organic light-emitting diodes from delayed fluorescence. *Nature*, 492(7428):234, 2012.

[57] Marc A Baldo, DF O'brien, Y You, A Shoustikov, et al. Highly efficient phosphorescent emission from organic electroluminescent devices. *Nature*, 395(6698):151, 1998.

[58] MA Baldo, S Lamansky, PE Burrows, ME Thompson, and SR Forrest. Very high-efficiency green organic light-emitting devices based on electrophosphorescence. *Applied Physics Letters*, 75(1):4–6, 1999.

[59] Tanya N Singh-Rachford and Felix N Castellano. Photon upconversion based on sensitized triplet–triplet annihilation. *Coordination Chemistry Reviews*, 254(21):2560–2573, 2010.

[60] DY Kondakov. Characterization of triplet-triplet annihilation in organic light-emitting diodes based on anthracene derivatives. *Journal of Applied Physics*, 102(11):114504, 2007.

[61] DY Kondakov, TD Pawlik, TK Hatwar, and JP Spindler. Triplet annihilation exceeding spin statistical limit in highly efficient fluorescent organic light-emitting diodes. *Journal of Applied Physics*, 106(12):124510, 2009.

[62] Fan Deng, Wenfang Sun, and Felix N Castellano. Texaphyrin sensitized near-ir-to-visible photon upconversion. *Photochemical & Photobiological Sciences*, 13(5):813–819, 2014.

[63] Taro Furukawa, Hajime Nakanotani, Munetomo Inoue, and Chihaya Adachi. Dual enhancement of electroluminescence efficiency and operational stability by rapid upconversion of triplet excitons in oleds. *Scientific reports*, 5:8429, 2015.

[64] Geoffrey B Piland, Jonathan J Burdett, Tzu-Yao Hung, Po-Hsun Chen, Chi-Feng Lin, Tien-Lung Chiu, Jiun-Haw Lee, and Christopher J Bardeen. Dynamics of molecular excitons near a semiconductor surface studied by fluorescence quenching of polycrystalline tetracene on silicon. *Chemical Physics Letters*, 601:33–38, 2014.

[65] Nicholas J Thompson, Mark WB Wilson, Daniel N Congreve, Patrick R Brown, Jennifer M Scherer, Thomas s Bischof, Mengfei Wu, Nadav Geva, Matthew Welborn, Troy Van Voorhis, et al. Energy harvesting of non-emissive triplet excitons in tetracene by emissive pbs nanocrystals. *Nature materials*, 13(11):1039, 2014.

[66] Sunpower solar cell (http://www.sunpowersolarcell.com/).

[67] Wendi Chang, Daniel N Congreve, Eric Hontz, Matthias E Bahlke, David P McMahon, Sebastian Reineke, Tony C Wu, Vladimir Bulovic, Troy Van Voorhis, and Marc A Baldo. Spin-dependent charge transfer state design rules in organic photovoltaics. *Nature communications*, 6:6415, 2015.

[68] Katsuaki Kawasumi, Tony Wu, Tianyu Zhu, Hyun Sik Chae, Troy Van Voorhis, Marc A Baldo, and Timothy M Swager. Thermally activated delayed fluorescence materials based on homoconjugation effect of donor–acceptor triptycenes. *Journal of the American Chemical Society*, 137(37):11908–11911, 2015.

[69] Gregory D Gutierrez, Graham T Sazama, Tony Wu, Marc A Baldo, and Timothy M Swager. Red phosphorescence from benzo [2, 1, 3] thiadiazoles at room temperature. *The Journal of organic chemistry*, 81(11):4789–4796, 2016.

[70] Aleksandr V Zhukhovitskiy, Michael G Mavros, KT Queeney, Tony Wu, Troy Van Voorhis, and Jeremiah A Johnson. Reactions of persistent carbenes with hydrogen-terminated silicon surfaces. *Journal of the American Chemical Society*, 138(27):8639–8652, 2016.

[71] Rafael Gómez-Bombarelli, Jorge Aguilera-Iparraguirre, Timothy D Hirzel, David Duvenaud, Dougal Maclaurin, Martin A Blood-Forsythe, Hyun Sik Chae, Markus Einzinger, Dong-Gwang Ha, Tony Wu, et al. Design of efficient molecular organic light-emitting diodes by a high-throughput virtual screening and experimental approach. *Nature Materials*, 15(10):1120–1127, 2016.